

Exact and model exchange-correlation potentials for open-shell systems

Bikash Kanungo,¹ Jeffrey Hatch,² Paul M. Zimmerman,² and Vikram Gavini^{1,3}

¹*Department of Mechanical Engineering, University of Michigan, Ann Arbor, Michigan 48109, USA*

²*Department of Chemistry, University of Michigan, Ann Arbor, Michigan 48109, USA*

³*Department of Materials Science and Engineering,
University of Michigan, Ann Arbor, Michigan 48109, USA*

The conventional approaches to the inverse density functional theory problem typically assume non-degeneracy of the Kohn-Sham (KS) eigenvalues, greatly hindering their use in open-shell systems. We present a generalization of the inverse density functional theory problem that can seamlessly admit degenerate KS eigenvalues. Additionally, we allow for fractional occupancy of the Kohn-Sham orbitals to also handle non-interacting ensemble- v -representable densities, as opposed to just non-interacting pure- v -representable densities. We present the exact exchange-correlation (XC) potentials for six open-shell systems—four atoms (Li, C, N, and O) and two molecules (CN and CH₂)—using accurate ground-state densities from configuration interaction calculations. We compare these exact XC potentials with model XC potentials obtained using non-local (B3LYP, SCAN0) and local/semi-local (SCAN, PBE, PW92) XC functionals. Although the relative errors in the densities obtained from these DFT functionals are of $\mathcal{O}(10^{-3} - 10^{-2})$, the relative errors in the model XC potentials remain substantially large— $\mathcal{O}(10^{-1} - 10^0)$.

Density functional theory [1, 2] (DFT) has become the most used electronic structure method due to its superior balance of speed and accuracy. Approximations to the exchange-correlation (XC) functional, however, limit DFT’s accuracy even though the theory itself is formally exact. A wide range of theoretical and empirical approaches have been proposed to improve the XC functional, but truly systematic means to doing so are wholly unknown. A promising alternative is to study the XC potential ($v_{xc}(\mathbf{r})$), which comes from the derivative of the XC functional. This information can be gained through the inverse DFT problem, which transforms the ground-state density (e.g. from an accurate wavefunction) into the XC potential. [3–9] This provides not only critical input data for conventional and machine-learning based XC approximations, [10, 11] but also the ability to probe deficiencies of existing model XC functionals. [12, 13]

Inverse DFT has been applied by our group [8, 13] and others [4, 6, 9, 14, 15] to electronic densities corresponding to spin singlet and predominantly closed shell states. The widespread interest in strongly correlated materials [16], including magnetic materials [17], superconductors [18], and transition metal based catalysts [19], however, puts a great distance between existing studies of XC potentials and materials systems of contemporary interest. As one key step towards bridging this divide, XC functionals must be modeled to handle open-shell systems accurately, where unpaired electrons are crucial. Prior algorithms for inverse DFT have not addressed this gap, though significant progress has been made in methods for closed shell electronic states.

The inverse DFT problem is solved as an iterative procedure [4, 5, 20–22] or constrained optimization [3, 6, 8, 14]. While most of these approaches suffer from numerical instabilities [14, 23, 24] and/or are based on electron densities with incorrect asymptotic behavior [8, 25–27], recent efforts have worked to address these challenges. In particular, one strategy uses the two-electron density

matrix instead of just the density [28–31] and another employs constrained optimization in a complete finite-element (FE) basis [8, 13]. The latter strategy finds XC potentials from densities containing correct asymptotics, giving highly accurate potentials that can be used in training XC functionals.

These above approaches have an implicit assumption of non-degeneracy in all or frontier Kohn-Sham (KS) eigenvalues, and hence, their applicability and robustness for systems with degenerate KS eigenvalues remain unclear. To elaborate, any inverse DFT algorithm relies on iterative updates to $v_{xc}(\mathbf{r})$ of the form $v_{xc}^{(n+1)}(\mathbf{r}) = v_{xc}^{(n)}(\mathbf{r}) + u^{(n)}(\mathbf{r})$, where $u^{(n)}(\mathbf{r})$ is defined in terms of the KS system and other auxiliary quantities (e.g., difference between KS and target density, adjoint functions, etc.) obtained using $v_{xc}^{(n)}(\mathbf{r})$. Given the non-uniqueness of the KS orbitals in case of degeneracy (i.e., one can choose any orthogonal transformation of the degenerate KS orbitals), there is non-uniqueness in the update $u^{(n)}$, leading to either non-convergence or “sloshing” of the XC potential. Thus, the conventional approaches to inverse DFT do not, in general, apply to open-shell systems, which can exhibit degeneracy in the KS eigenvalues.

We propose a reformulation of the partial differential equation (PDE) constrained optimization approach to the inverse DFT problem [8, 9, 15] which guarantees a unique update to $v_{xc}(\mathbf{r})$ at each iteration. Given the target spin densities $\rho_{\sigma}^{\text{data}}(\mathbf{r})$ (with $\sigma = 1, 2$ being the spin index), the inverse DFT problem of finding the $v_{xc,\sigma}(\mathbf{r})$ that yields the target densities can be posed as the following PDE-constrained optimization:

$$\min_{\{v_{xc,\sigma}(\mathbf{r})\}} \sum_{\sigma=1}^2 \int (\rho_{\sigma}^{\text{data}}(\mathbf{r}) - \rho_{\sigma}(\mathbf{r}))^2 d\mathbf{r}, \quad (1)$$

where $\rho_{\sigma}(\mathbf{r})$ are the KS spin densities obtained from the solutions of the KS eigenvalue problem, which, for a non-

periodic system (e.g., atoms, molecules), is given by

$$\hat{\mathcal{H}}_\sigma \Psi_{k,\sigma}(\mathbf{r}) = \Psi_{k,\sigma}(\mathbf{r}) \mathbf{E}_{k,\sigma}, \quad k = 1, 2, \dots, M_\sigma. \quad (2)$$

In the above equation, $\hat{\mathcal{H}}_\sigma = -\frac{1}{2}\nabla^2 + v_H(\mathbf{r}) + v_N(\mathbf{r}) + v_{xc,\sigma}(\mathbf{r})$ is the KS Hamiltonian for spin index σ ; k indexes the distinct eigenvalues, with the k^{th} eigenvalue having a multiplicity of $m_{k,\sigma}$. $\mathbf{E}_{k,\sigma} = \epsilon_{k,\sigma} \mathbf{I}_{m_{k,\sigma}}$ is the diagonal eigenvalue matrix, with $\epsilon_{k,\sigma}$ as the k^{th} distinct eigenvalue. $\Psi_{k,\sigma}(\mathbf{r}) = [\psi_{k,\sigma}^{(1)}(\mathbf{r}) \mid \psi_{k,\sigma}^{(2)}(\mathbf{r}) \mid \dots \mid \psi_{k,\sigma}^{(m_{k,\sigma})}(\mathbf{r})]$ comprises of the $m_{k,\sigma}$ real-valued degenerate eigenfunctions. Although the formulation presented here is for non-periodic systems, the main ideas can also be extended to periodic systems. Typically, one is interested in the canonical eigenfunction, which are orthonormal. The orthogonality between eigenfunctions belonging to different eigenvalues is guaranteed by the Hermiticity of the KS Hamiltonian. Thus, to obtain the canonical eigenfunctions, we enforce orthonormality among degenerate eigenfunctions, which can be expressed as

$$\int \Psi_{k,\sigma}^T(\mathbf{r}) \Psi_{k,\sigma}(\mathbf{r}) d\mathbf{r} = \mathbf{I}_{m_{k,\sigma}}. \quad (3)$$

Given the canonical eigenfunctions $\{\Psi_{k,\sigma}\}_{k=1}^{M_\sigma}$, its spin

density can be defined as

$$\rho_\sigma(\mathbf{r}) = \sum_{k=1}^{M_\sigma} \text{Tr} \left(f(\mathbf{E}_{k,\sigma}) \Psi_{k,\sigma}^T(\mathbf{r}) \Psi_{k,\sigma}(\mathbf{r}) \right), \quad (4)$$

where $f(\mathbf{E}_{k,\sigma}) = (\mathbf{I}_{m_{k,\sigma}} + e^{-(\mathbf{E}_{k,\sigma} - \mu \mathbf{I}_{m_{k,\sigma}})/k_B T})^{-1}$ is Fermi-Dirac occupancy matrix with μ being the chemical potential of the system given through the conservation of the number of electrons (N_e),

$$\sum_{\sigma} \sum_{k=1}^{M_\sigma} \text{Tr} (f(\mathbf{E}_{k,\sigma})) = N_e. \quad (5)$$

The use of occupancy is crucial to seamlessly handle both non-interacting pure-v-representable (pure- v_s) and ensemble-v-representable (e- v_s) densities—densities corresponding to a single or an ensemble of KS determinants, respectively. In general it is difficult to *a priori* ascertain if a target density is pure- v_s or e- v_s . To this end, the use of occupancy allows a unified means to admit both kinds of densities. Using the various constraints (Eqs. 2, 3, and 5), the optimization in Eq. 1 can be recast as an unconstrained optimization of the Lagrangian,

$$\begin{aligned} \mathcal{L} = & \sum_{\sigma} \int (\rho_{\sigma}^{\text{data}}(\mathbf{r}) - \rho_{\sigma}(\mathbf{r}))^2 d\mathbf{r} + \sum_{\sigma} \sum_{k=1}^{M_\sigma} \text{Tr} \left(\int \mathbf{P}_{k,\sigma}^T(\mathbf{r}) \left(\hat{\mathcal{H}}_\sigma \Psi_{k,\sigma}(\mathbf{r}) - \Psi_{k,\sigma}(\mathbf{r}) \mathbf{E}_{k,\sigma} \right) d\mathbf{r} \right) + \\ & \eta \left(\sum_{\sigma} \sum_{k=1}^{M_\sigma} \text{Tr} (f(\mathbf{E}_{k,\sigma})) - N_e \right) + \sum_{\sigma} \sum_{k=1}^{M_\sigma} \text{Tr} \left(\mathbf{D}_{k,\sigma} \left(\int \Psi_{k,\sigma}^T(\mathbf{r}) \Psi_{k,\sigma}(\mathbf{r}) d\mathbf{r} - \mathbf{I}_{m_{k,\sigma}} \right) \right), \end{aligned} \quad (6)$$

where $\mathbf{P}_{k,\sigma}(\mathbf{r}) = [p_{k,\sigma}^{(1)}(\mathbf{r}) \mid p_{k,\sigma}^{(2)}(\mathbf{r}) \mid \dots \mid p_{k,\sigma}^{(m_{k,\sigma})}(\mathbf{r})]$ comprises of the adjoint functions that enforce the constraints corresponding to the KS eigenvalue problem (Eq. 2); $\mathbf{D}_{k,\sigma} \in \mathbb{R}^{m_{k,\sigma} \times m_{k,\sigma}}$ is the Lagrange multiplier matrix enforcing the orthonormality constraints in Eq. 3; $\eta \in \mathbb{R}$

is the Lagrange multiplier enforcing Eq. 5. Optimizing \mathcal{L} with respect to $\mathbf{P}_{k,\sigma}$, $\mathbf{D}_{k,\sigma}$ and η , yields the constraints equations Eq. 2, Eq. 3, and Eq. 5, respectively. Optimizing \mathcal{L} with respect to $\Psi_{k,\sigma}$, $\mathbf{E}_{k,\sigma}$, and μ results in:

$$\hat{\mathcal{H}}_\sigma(\mathbf{r}) \mathbf{P}_{k,\sigma} - \mathbf{P}_{k,\sigma} \mathbf{E}_{k,\sigma} = 4 (\rho_{\sigma}^{\text{data}}(\mathbf{r}) - \rho_{\sigma}(\mathbf{r})) \Psi_{k,\sigma}(\mathbf{r}) f(\mathbf{E}_{k,\sigma}) - \Psi_{k,\sigma}(\mathbf{r}) (\mathbf{D}_{k,\sigma} + \mathbf{D}_{k,\sigma}^T), \quad (7)$$

$$\int \Psi_{k,\sigma}^T(\mathbf{r}) \mathbf{P}_{k,\sigma}(\mathbf{r}) d\mathbf{r} = \frac{\partial f_{k,\sigma}^{\mu}}{\partial \epsilon_{k,\sigma}} \left[-2 \int (\rho_{\sigma}^{\text{data}}(\mathbf{r}) - \rho_{\sigma}(\mathbf{r})) \Psi_{k,\sigma}^T(\mathbf{r}) \Psi_{k,\sigma}(\mathbf{r}) d\mathbf{r} + \eta \mathbf{I}_{m_{k,\sigma}} \right], \quad (8)$$

$$\eta \sum_{\sigma} \sum_{k=1}^{M_\sigma} m_{k,\sigma} \frac{\partial f_{k,\sigma}^{\mu}}{\partial \mu} = 2 \sum_{\sigma} \sum_{k=1}^{M_\sigma} \frac{\partial f_{k,\sigma}^{\mu}}{\partial \mu} \int (\rho_{\sigma}^{\text{data}}(\mathbf{r}) - \rho_{\sigma}(\mathbf{r})) \text{Tr} \left(\Psi_{k,\sigma}^T(\mathbf{r}) \Psi_{k,\sigma}(\mathbf{r}) \right) d\mathbf{r}, \quad (9)$$

where $f_{k,\sigma}^{\mu} = (1 + e^{-(\epsilon_{k,\sigma} - \mu)/k_B T})^{-1}$. Having solved

Eqs. 2, 3, 5, 7, 8, and 9, we can write

$$\frac{\delta \mathcal{L}}{\delta v_{xc,\sigma}(\mathbf{r})} = \sum_{k=1}^{M_\sigma} \text{Tr} \left(\mathbf{P}_{k,\sigma}^T(\mathbf{r}) \Psi_{k,\sigma}(\mathbf{r}) \right). \quad (10)$$

The above provides the update to $v_{xc,\sigma}(\mathbf{r})$ to be used in any gradient-based optimization method. In the case of degeneracy, $\Psi_{k,\sigma}$ cannot be determined uniquely. That is any $\tilde{\Psi}_{k,\sigma} = \Psi_{k,\sigma} \mathbf{Q}_{k,\sigma}$ (with $\mathbf{Q}_{k,\sigma}$ being any $m_{k,\sigma} \times m_{k,\sigma}$ orthogonal matrix) will satisfy Eqs. 2, 3 as well as preserve the density (Eq. 4). However, using $\tilde{\Psi}_{k,\sigma}$ in the adjoint equation (Eq. 7), the corresponding adjoint is given by $\tilde{\mathbf{P}}_{k,\sigma} = \mathbf{P}_{k,\sigma} \mathbf{Q}_{k,\sigma}$. Thus for any orthogonal transformation of $\Psi_{k,\sigma}$, its corresponding adjoint functions also are transformed similarly. Finally, rewriting Eq. 10 in terms of $\tilde{\Psi}_{k,\sigma}$ and $\tilde{\mathbf{P}}_{k,\sigma}$, we have

$$\begin{aligned} \frac{\delta \mathcal{L}}{\delta v_{xc,\sigma}(\mathbf{r})} &= \sum_{k=1}^{M_\sigma} \text{Tr} \left(\tilde{\mathbf{P}}_{k,\sigma}^\text{T}(\mathbf{r}) \tilde{\Psi}_{k,\sigma}(\mathbf{r}) \right) \\ &= \sum_{k=1}^{M_\sigma} \text{Tr} \left(\mathbf{Q}_{k,\sigma}^\text{T} \mathbf{P}_{k,\sigma}^\text{T}(\mathbf{r}) \Psi_{k,\sigma}(\mathbf{r}) \mathbf{Q}_{k,\sigma} \right) \quad (11) \\ &= \sum_{k=1}^{M_\sigma} \text{Tr} \left(\mathbf{P}_{k,\sigma}^\text{T}(\mathbf{r}) \Psi_{k,\sigma}(\mathbf{r}) \right), \end{aligned}$$

where we used the invariance of the trace of products of matrices with respect to cyclic permutations. This shows the uniqueness of $\delta \mathcal{L} / \delta v_{xc,\sigma}(\mathbf{r})$ for a given $v_{xc,\sigma}(\mathbf{r})$. We refer to the Supplemental Material [32] for a detailed derivation of Eqs. 7–11.

In order to numerically solve the above equations, we discretize the $\Psi_{k,\sigma}$ and $v_{xc,\sigma}$ using an adaptively refined finite-element basis [33–35] that provides systematic convergence for all-electron DFT calculations, and is essential for an accurate solution of the inverse DFT problem. In particular, we use an adaptive discretization based on a fourth-order spectral finite-element (FE) basis for discretizing the KS eigenfunctions and the corresponding adjoint functions. A discretization based on linear finite-element basis is sufficient for $v_{xc,\sigma}$, which is a smoother field in comparison to the KS eigenfunctions. To mitigate the unphysical artifacts in $v_{xc,\sigma}$ from the incorrect asymptotics in the Gaussian target densities (i.e., lack of cusp on the nuclei and Gaussian decay instead of exponential decay in the far-field), we: (a) add a small cusp-correction to $\rho_\sigma^\text{data}(\mathbf{r})$ near the nuclei, and (b) enforce appropriate boundary condition on $v_{xc,\sigma}(\mathbf{r})$ in the low density region ($\rho_\sigma^\text{data}(\mathbf{r}) < 10^{-7}$). We refer to [8, 13] for details of the FE basis and the asymptotic corrections.

We compare exact and model XC potentials for four atoms—Li (doublet), C (triplet, $\nu = 2$), N (quartet, $\nu = 3$), and O (triplet, $\nu = 2$), where ν denotes the difference in the number of majority (up) and minority (down) spin electrons. Additionally, we also consider two molecules—CN (doublet) and CH₂ (triplet, $\nu = 2$). The exact $v_{xc,\sigma}(\mathbf{r})$ are obtained using ground state densities from heat-bath configuration interactions (HBCI) calculations [10]. The model $v_{xc,\sigma}$ potentials are obtained using DFT-based ground state densities of widely used approximate XC functionals, which includes two hybrid (B3LYP [37, 38] and SCAN0 [39]), one meta-

GGA (SCAN [40]), one GGA (PBE [41]), and one LDA (PW92 [42]) functional. All the HBCI and DFT calculations are done using the QChem software package [11] with a polarized, quadruple zeta with tight core Gaussian basis set (cc-pCVQZ) [44]. For all inverse DFT calculations, we use a temperature $T = 100$ K for the Fermi-Dirac distribution. We remark that while the use of a non-zero temperature formally results in an e - v_s density, practically, for systems with non-degenerate frontier orbitals or with finite HOMO-LUMO gap, it results in a pure- v_s density. The L_2 error in the density— $\|\rho_\sigma^\text{data} - \rho_\sigma\|_{L_2}$ —is driven below 10^{-4} (except for B3LYP, where it is driven below 3×10^{-4}) at convergence. We quantify the difference between the exact and the model XC potentials using two ρ_σ^data weighted error metrics

$$e_{1,\sigma} = \frac{\|\rho_\sigma^\text{data} \delta v_{xc,\sigma}\|_{L_2}}{\|\rho_\sigma^\text{data} v_{xc,\sigma}^\text{exact}\|_{L_2}}, \quad e_{2,\sigma} = \frac{\|\rho_\sigma^\text{data} |\nabla \delta v_{xc,\sigma}|\|_{L_2}}{\|\rho_\sigma^\text{data} |\nabla v_{xc,\sigma}^\text{exact}|\|_{L_2}}, \quad (12)$$

where $\delta v_{xc,\sigma} = v_{xc,\sigma}^\text{exact} - v_{xc,\sigma}^\text{model}$ (cf. Supplemental Material for error metrics without the ρ_σ^data weight). For all the open-shell systems considered, the target densities (from HBCI and DFT) turn out to be pure- v_s densities. However, to test the efficacy of the proposed approach in handling e - v_s density, we used a SCAN0 based density for the B atom obtained using a Fermi-Dirac smearing in the ground state calculation. Upon inversion, the density leads to an ensemble of KS single Slater determinants for the majority-spin—three degenerate orbitals near the Fermi level with 1/3 occupancy (see Supplemental Material [32] for details).

Fig. 1 compares the exact and model XC potentials corresponding to B3LYP, SCAN0, and SCAN densities (all majority-spin), for C and O. The model potentials differ significantly in the low density region, owing to their incorrect far-field asymptotics. Importantly, the model potentials differ qualitatively even in the high density region. All the model XC potentials are deeper at the atoms compared to the exact one (see insets in Fig. 1), with the B3LYP potential being substantially deeper. The SCAN0 and SCAN based model potentials exhibit the atomic inter-shell structure—a distinctive feature of the exact potential marked by a local maxima to minima transition—otherwise absent in the B3LYP potentials (see left insets in Fig. 1). Quantitatively, SCAN0 based potentials provide better agreement with the exact one (see Table I) than other model potentials. While the relative L_2 errors in densities for the model functionals are of $\mathcal{O}(10^{-3} - 10^{-2})$, the relative errors in the XC potentials are of $\mathcal{O}(10^{-1} - 10^0)$, manifesting in significant differences in the KS eigenvalues, especially for the minority-spin (cf. Supplemental Material [32]). In other words, for assessing the XC functionals, the XC potentials are more descriptive than the densities. This presents a strong case for using the exact XC potentials in the design and modeling of XC functionals.

Turning to the molecules, Fig. 2 compares the exact

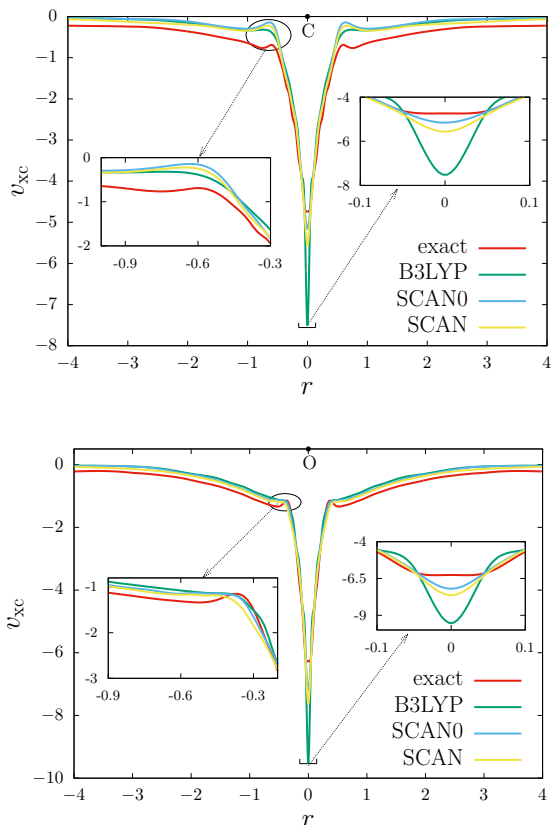


FIG. 1. Comparison of exact and model XC potentials for C (top) and O (bottom) atoms for the majority-spin. The x-axis corresponds to the dominant principal axis of the moment of inertia tensor of their densities.

and model XC potentials for CN (majority-spin). For CH_2 , Fig. 3 presents the error ($v_{xc,\sigma}^{\text{exact}} - v_{xc,\sigma}^{\text{model}}$) in the B3LYP and SCAN0 based XC potentials (cf. Supplemental Material for a similar comparison for SCAN and the individual $v_{xc,\sigma}$). Similar to the atoms, the model potentials are deeper at the atoms. Once again, SCAN0 and SCAN based potentials offer better qualitative and quantitative agreement than the rest, including the presence of atomic intershell structure around both C and N atom in CN and around the C atom in CH_2 (cf. yellow rings around the C atom in the $v_{xc,\sigma}$ plots for CH_2 in the Supplemental Material [32]). Results for minority-spin counterparts of Figs. 1-3 as well as Li and N can be found in the Supplemental Material [32].

By generalizing the inverse DFT approach to degenerate KS eigenvalues and ensemble- v -representable densities, new insights into the XC potential for open-shell electronic states can be gained. First, this allowed comparisons to be made between exact and model XC potentials, providing a quantitative measure of the quality of model XC potentials for open-shell states. The availability of exact XC potentials for the open-shell case will serve as an important guide for the creation of new, accurate models of XC within DFT.

We gratefully acknowledge DOE grant DE-SC0022241

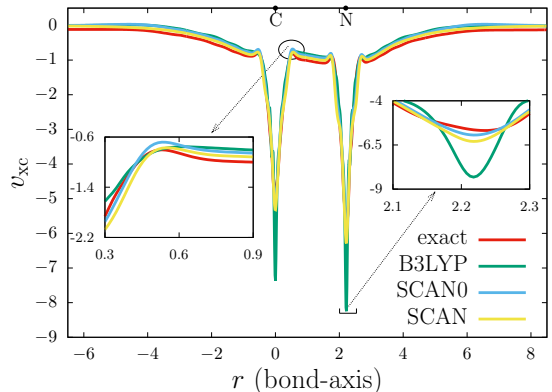


FIG. 2. Comparison of exact and model XC potentials for CN along the bond for the majority-spin.

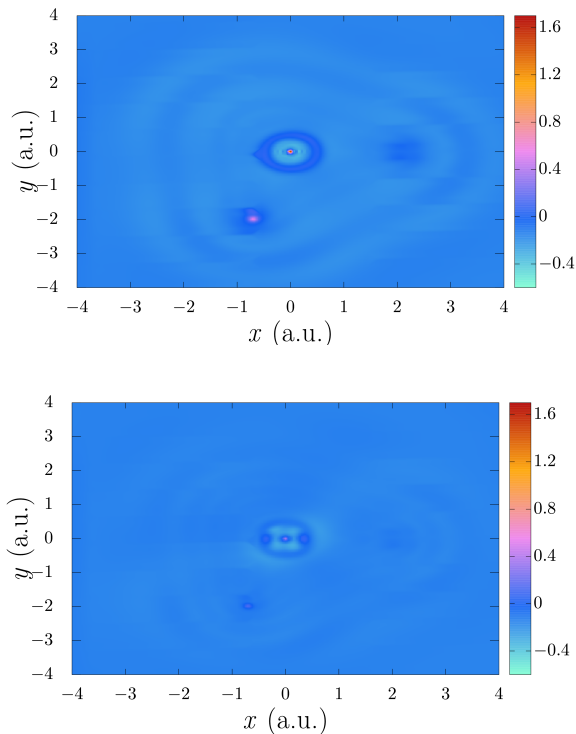


FIG. 3. Error in the B3LYP (top) and SCAN0 (bottom) based model XC potentials for CH_2 on the plane of the molecule.

which supported this study. V.G. also acknowledges support from AFOSR grant FA9550-21-1-0302 that supported the analysis of degenerate eigenvalue problems. This research used resources of the NERSC Center, a DOE Office of Science User Facility supported by the Office of Science of the U.S. Department of Energy under Contract No. DE-AC02-05CH11231. We acknowledge the support of DURIP grant W911NF1810242, which also provided computational resources for this work.

TABLE I. Comparison of the model XC potentials in terms of the error metrics $e_{1,\sigma}$ and $e_{2,\sigma}$ (defined in Eq. 12), for the majority-spin. See the Supplemental Material [32] for the error metrics for minority-spin.

Model	Li		C		N		O		CN		CH ₂	
	$e_{1,\sigma}$	$e_{2,\sigma}$	$e_{1,\sigma}$	$e_{2,\sigma}$	$e_{1,\sigma}$	$e_{2,\sigma}$	$e_{1,\sigma}$	$e_{2,\sigma}$	$e_{1,\sigma}$	$e_{2,\sigma}$	$e_{1,\sigma}$	$e_{2,\sigma}$
B3LYP	0.716	0.816	0.788	0.413	0.776	0.507	0.775	0.389	0.768	0.373	0.778	0.681
SCAN0	0.676	0.83	0.743	0.363	0.73	0.461	0.727	0.294	0.723	0.278	0.736	0.677
SCAN	0.877	0.833	0.907	0.34	0.915	0.572	0.922	0.318	0.909	0.337	0.912	0.709
PBE	0.869	1.002	0.895	0.483	0.906	0.476	0.918	0.437	0.905	0.478	0.904	0.761
PW92	0.875	0.852	0.905	0.406	0.915	0.467	0.922	0.426	0.908	0.409	0.911	0.735

-
- [1] P. Hohenberg and W. Kohn, Phys. Rev. **136**, B864 (1964).
- [2] W. Kohn and L. J. Sham, Phys. Rev. **140**, A1133 (1965).
- [3] Q. Zhao, R. C. Morrison, and R. G. Parr, Phys. Rev. A **50**, 2138 (1994).
- [4] R. van Leeuwen and E. J. Baerends, Phys. Rev. A **49**, 2421 (1994).
- [5] K. Peirs, D. Van Neck, and M. Waroquier, Phys. Rev. A **67**, 012505 (2003).
- [6] Q. Wu and W. Yang, J. Chem. Phys. **118**, 2498 (2003).
- [7] D. S. Jensen and A. Wasserman, Int. J. Quantum Chem. **118**, e25425 (2018).
- [8] B. Kanungo, P. M. Zimmerman, and V. Gavini, Nat. Commun. **10**, 4497 (2019).
- [9] Y. Shi and A. Wasserman, J. Phys. Chem. Lett. **12**, 5308 (2021).
- [10] J. Schmidt, C. L. Benavides-Riveros, and M. A. Marques, J. Phys. Chem. Lett. **10**, 6425 (2019).
- [11] Y. Zhou, J. Wu, S. Chen, and G. Chen, J. Phys. Chem. Lett. **10**, 7264 (2019).
- [12] S. Nam, S. Song, E. Sim, and K. Burke, J. Chem. Theory Comput. **16**, 5014 (2020).
- [13] B. Kanungo, P. M. Zimmerman, and V. Gavini, J. Phys. Chem. Lett. **12**, 12012 (2021).
- [14] C. R. Jacob, J. Chem. Phys. **135**, 244102 (2011).
- [15] Y. Shi, V. H. Chávez, and A. Wasserman, Wiley Interdisciplinary Reviews: Computational Molecular Science **12**, e1617 (2022).
- [16] E. Dagotto, Science **309**, 257 (2005).
- [17] J. P. Malrieu, R. Caballol, C. J. Calzado, C. De Graaf, and N. Guihery, Chemical reviews **114**, 429 (2014).
- [18] J. Orenstein and A. Millis, Science **288**, 468 (2000).
- [19] J. Paier, C. Penschke, and J. Sauer, Chemical reviews **113**, 3949 (2013).
- [20] A. Görling, Physical Review A **46**, 3753 (1992).
- [21] Y. Wang and R. G. Parr, Phys. Rev. A **47**, R1591 (1993).
- [22] I. G. Ryabinkin and V. N. Staroverov, J. Chem. Phys. **137**, 164113 (2012).
- [23] T. Heaton-Burgess, F. A. Bulat, and W. Yang, Phys. Rev. Lett. **98**, 256401 (2007).
- [24] F. A. Bulat, T. Heaton-Burgess, A. J. Cohen, and W. Yang, J. Chem. Phys. **127**, 174101 (2007).
- [25] M. E. Mura, P. J. Knowles, and C. A. Reynolds, J. Chem. Phys. **106**, 9659 (1997).
- [26] P. R. T. Schipper, O. V. Gritsenko, and E. J. Baerends, Theor. Chem. Acc. **98**, 16 (1997).
- [27] A. P. Gaiduk, I. G. Ryabinkin, and V. N. Staroverov, J. Chem. Theory Comput. **9**, 3959 (2013).
- [28] I. G. Ryabinkin, S. V. Kohut, and V. N. Staroverov, Phys. Rev. Lett. **115**, 083001 (2015).
- [29] R. Cuevas-Saavedra, P. W. Ayers, and V. N. Staroverov, J. Chem. Phys. **143**, 244116 (2015).
- [30] E. Ospadov, I. G. Ryabinkin, and V. N. Staroverov, J. Chem. Phys. **146**, 084103 (2017).
- [31] S. Tribedi, D.-K. Dang, B. Kanungo, V. Gavini, and P. M. Zimmerman, arXiv:2302.11999 (2023).
- [32] Supplementary Material - URL_to_be_inserted_by_publisher.
- [33] P. Motamarri, M. Nowak, K. Leiter, J. Knap, and V. Gavini, Journal of Computational Physics **253**, 308 (2013).
- [34] P. Motamarri, S. Das, S. Rudraraju, K. Ghosh, D. Davydov, and V. Gavini, Comput. Phys. Commun. **246**, 106853 (2020).
- [35] S. Das, P. Motamarri, V. Subramanian, D. M. Rogers, and V. Gavini, Comput. Phys. Commun. **280**, 108473 (2022).
- [10] D.-K. Dang, J. A. Kammeraad, and P. M. Zimmerman, J. Phys. Chem. **127**, 400 (2023).
- [37] A. D. Becke, J. Chem. Phys. **98**, 5648 (1993).
- [38] C. Lee, W. Yang, and R. G. Parr, Phys. Rev. B **37**, 785 (1988).
- [39] K. Hui and J.-D. Chai, J. Chem. Phys. **144**, 044114 (2016).
- [40] J. Sun, A. Ruzsinszky, and J. P. Perdew, Phys. Rev. Lett. **115**, 036402 (2015).
- [41] J. P. Perdew, K. Burke, and M. Ernzerhof, Phys. Rev. Lett. **77**, 3865 (1996).
- [42] J. P. Perdew and Y. Wang, Phys. Rev. B **45**, 13244 (1992).
- [11] Y. Shao et al, Mol. Phys. **113**, 184 (2015).
- [44] B. P. Pritchard, D. Altarawy, B. Didier, T. D. Gibson, and T. L. Windus, J. Chem. Inf. Model. **59**, 4814 (2019).

Supplemental Material

S1. OPTIMALITY CONDITIONS

In this section we derive the optimality conditions (Eqs. 7, 8, and 9 in the main manuscript) and provide the details of their solution procedure. First, we begin with a relation that will be useful subsequently.

- Given the matrix function $f(\mathbf{E}) = (\mathbf{I} + e^{-(\mathbf{E}-\mu\mathbf{I})/k_B T})^{-1}$,

$$\frac{\partial f(\mathbf{E})}{\partial E_{ij}} = \frac{1}{k_B T} \left(\mathbf{I} + e^{-(\mathbf{E}-\mu\mathbf{I})/k_B T} \right)^{-1} e^{-(\mathbf{E}-\mu\mathbf{I})/k_B T} \left(\Lambda^{ij} + \frac{1}{2k_B T} [\mathbf{E}, \Lambda^{ij}] \right) \left(\mathbf{I} + e^{-(\mathbf{E}-\mu\mathbf{I})/k_B T} \right)^{-1}, \quad (\text{S1})$$

where $[\mathbf{A}, \mathbf{B}] = \mathbf{AB} - \mathbf{BA}$ is the commutator of two matrices and Λ^{ij} is a matrix which is zero except in the (i, j) -th entry, which is equal to 1. In other words, $(\Lambda^{ij})_{kl} = \delta_{ik}\delta_{jl}$.

Proof. The proof of the above follows from the following definition of $\frac{\partial f(\mathbf{E})}{\partial E_{ij}}$ in terms of a directional derivative along Λ^{ij} ,

$$\frac{\partial f(\mathbf{E})}{\partial E_{ij}} = \lim_{h \rightarrow 0} \frac{f(\mathbf{E} + h\Lambda^{ij}) - f(\mathbf{E})}{h}. \quad (\text{S2})$$

Using the definition of $f(\mathbf{E})$,

$$f(\mathbf{E} + h\Lambda^{ij}) = \left(\mathbf{I} + e^{-(\mathbf{E} + h\Lambda^{ij} - \mu\mathbf{I})/k_B T} \right)^{-1} = \left(\mathbf{I} + e^{\mu/k_B T} e^{-(\mathbf{E} + h\Lambda^{ij})/k_B T} \right)^{-1}, \quad (\text{S3})$$

where the last equality follows from the fact that $\mu\mathbf{I}$ commutes with $(\mathbf{E} + h\Lambda^{ij})$ (Note: If $[\mathbf{A}, \mathbf{B}] = 0$, $e^{\mathbf{A}+\mathbf{B}} = e^{\mathbf{A}}e^{\mathbf{B}}$). Letting, $s = e^{\mu/k_B T}$ and $t = 1/k_B T$,

$$\begin{aligned} f(\mathbf{E} + h\Lambda^{ij}) &= \left(\mathbf{I} + se^{-t(\mathbf{E} + h\Lambda^{ij})} \right)^{-1} \\ &= \left(\mathbf{I} + se^{-t\mathbf{E}} e^{-ht\Lambda^{ij}} e^{-\frac{ht^2}{2}[\mathbf{E}, \Lambda^{ij}]} e^{-\frac{h^2 t^3}{6}(2[\Lambda^{ij}, [\mathbf{E}, \Lambda^{ij}]] + [\mathbf{E}, [\mathbf{E}, \Lambda^{ij}]])} \dots \right)^{-1} \\ &= \left(\mathbf{I} + se^{-t\mathbf{E}} \left(\mathbf{I} - ht \left(\Lambda^{ij} + \frac{t}{2} [\mathbf{E}, \Lambda^{ij}] \right) + \mathcal{O}(h^2) \right) \right)^{-1} \\ &= \left(\mathbf{I} + se^{-t\mathbf{E}} - htse^{-t\mathbf{E}} \left(\Lambda^{ij} + \frac{t}{2} [\mathbf{E}, \Lambda^{ij}] \right) + \mathcal{O}(h^2) \right)^{-1} \end{aligned} \quad (\text{S4})$$

where in the second equality we used the Zassenhaus formula [S1]. For two square matrices \mathbf{A} and \mathbf{B} of same dimensions, $(\mathbf{A} - \mathbf{B})^{-1} = \sum_{l=0}^{\infty} (\mathbf{A}^{-1}\mathbf{B})^l \mathbf{A}^{-1}$. Taking $\mathbf{A} = \mathbf{I} + se^{-t\mathbf{E}}$ and $\mathbf{B} = htse^{-t\mathbf{E}} (\Lambda^{ij} + \frac{t}{2} [\mathbf{E}, \Lambda^{ij}]) + \mathcal{O}(h^2)$, the above equation yields,

$$\begin{aligned} f(\mathbf{E} + h\Lambda^{ij}) &= (\mathbf{I} + se^{-t\mathbf{E}})^{-1} + (\mathbf{I} + se^{-t\mathbf{E}})^{-1} \left(htse^{-t\mathbf{E}} \left(\Lambda^{ij} + \frac{t}{2} [\mathbf{E}, \Lambda^{ij}] \right) \right) (\mathbf{I} + se^{-t\mathbf{E}})^{-1} \\ &\quad + \mathcal{O}(h^2). \end{aligned} \quad (\text{S5})$$

Using the above relation in Eq. S2 gives,

$$\frac{\partial f(\mathbf{E})}{\partial E_{ij}} = ts (\mathbf{I} + se^{-t\mathbf{E}})^{-1} e^{-t\mathbf{E}} \left(\Lambda^{ij} + \frac{t}{2} [\mathbf{E}, \Lambda^{ij}] \right) (\mathbf{I} + se^{-t\mathbf{E}})^{-1}. \quad (\text{S6})$$

This concludes the derivation of Eq. S1.

A. Derivation of Eq. 7 in the main manuscript

Taking the variation of a \mathcal{L} with respect to a KS orbital $\psi_{k,\sigma}^{(i)}$, we have

$$\frac{\delta \mathcal{L}}{\delta \psi_{k,\sigma}^{(i)}(\mathbf{r})} = -2(\rho_\sigma^{\text{data}}(\mathbf{r}) - \rho_\sigma(\mathbf{r})) \frac{\partial \rho_\sigma(\mathbf{r})}{\partial \psi_{k,\sigma}^{(i)}(\mathbf{r})} + \hat{\mathcal{H}}_\sigma p_{k,\sigma}^{(i)}(\mathbf{r}) - \sum_j^{m_{k,\sigma}} p_{j,\sigma}^{(j)}(\mathbf{r}) E_{ij} + \sum_{j=1}^{m_{k,\sigma}} (D_{k,\sigma,ij} + D_{k,\sigma,ji}) \psi_{k,\sigma}^{(j)}. \quad (\text{S7})$$

Using $\rho_\sigma(\mathbf{r}) = \sum_{k=1}^{M_\sigma} \text{Tr} \left(f(\mathbf{E}_{k,\sigma}) \Psi_{k,\sigma}^T(\mathbf{r}) \Psi_{k,\sigma}(\mathbf{r}) \right)$, we have

$$\frac{\partial \rho_\sigma(\mathbf{r})}{\partial \psi_{k,\sigma}^{(i)}(\mathbf{r})} = \sum_j^{m_{k,\sigma}} (f(\mathbf{E}_{k,\sigma})_{ij} + f(\mathbf{E}_{k,\sigma})_{ji}) \psi_{k,\sigma}^{(j)}(\mathbf{r}) = 2 \sum_j^{m_{k,\sigma}} f(\mathbf{E}_{k,\sigma})_{ij} \psi_{k,\sigma}^{(j)}(\mathbf{r}), \quad (\text{S8})$$

where the last equality uses the fact that $f(\mathbf{E}_{k,\sigma})$ is a symmetric matrix. Now, using the above relation in Eq. S7 and setting $\frac{\delta \mathcal{L}}{\delta \psi_{k,\sigma}^{(i)}(\mathbf{r})}$ to zero gives

$$\hat{\mathcal{H}}_\sigma p_{k,\sigma}^{(i)}(\mathbf{r}) - \sum_j^{m_{k,\sigma}} p_{j,\sigma}^{(j)}(\mathbf{r}) E_{ij} = 4(\rho_\sigma^{\text{data}}(\mathbf{r}) - \rho_\sigma(\mathbf{r})) \sum_j^{m_{k,\sigma}} f(\mathbf{E}_{k,\sigma})_{ij} \psi_{k,\sigma}^{(j)}(\mathbf{r}) - \sum_{j=1}^{m_{k,\sigma}} (D_{k,\sigma,ij} + D_{k,\sigma,ji}) \psi_{k,\sigma}^{(j)}. \quad (\text{S9})$$

Combining the above for all the degenerate $\psi_{k,\sigma}^{(i)}$'s results in

$$\hat{\mathcal{H}}_\sigma \mathbf{P}_{k,\sigma}(\mathbf{r}) - \mathbf{P}_{k,\sigma} \mathbf{E}_{k,\sigma} = 4(\rho_\sigma^{\text{data}}(\mathbf{r}) - \rho_\sigma(\mathbf{r})) \Psi_{k,\sigma}(\mathbf{r}) f(\mathbf{E}_{k,\sigma}) - \Psi_{k,\sigma}(\mathbf{r}) (\mathbf{D}_{k,\sigma} + \mathbf{D}_{k,\sigma}^T), \quad (\text{S10})$$

same as Eq. 7 of the main manuscript.

B. Derivation of Eq. 8 in the main manuscript

Let $E_{k,\sigma}^{ij}$ be the (i, j) -th entry of $\mathbf{E}_{k,\sigma}$. Taking the partial derivative of \mathcal{L} with $E_{k,\sigma}^{ij}$, we have

$$\frac{\partial \mathcal{L}}{\partial E_{k,\sigma}^{ij}} = -2 \int (\rho_\sigma^{\text{data}}(\mathbf{r}) - \rho_\sigma(\mathbf{r})) \text{Tr} \left(\frac{\partial f(\mathbf{E}_{k,\sigma})}{\partial E_{k,\sigma}^{ij}} \Psi_{k,\sigma}^T(\mathbf{r}) \Psi_{k,\sigma}(\mathbf{r}) \right) d\mathbf{r} + \eta \text{Tr} \left(\frac{\partial f(\mathbf{E}_{k,\sigma})}{\partial E_{k,\sigma}^{ij}} \right) - \int \psi_{k,\sigma}^{(i)}(\mathbf{r}) p_{k,\sigma}^{(j)}(\mathbf{r}) d\mathbf{r}. \quad (\text{S11})$$

We now use Eq. S1 to simplify the above equation. Substituting $\mathbf{E} = \mathbf{E}_{k,\sigma}$ in Eq. S1,

$$\begin{aligned} \frac{\partial f(\mathbf{E}_{k,\sigma})}{\partial E_{k,\sigma}^{ij}} &= \frac{1}{k_B T} \left(\mathbf{I}_{m_{k,\sigma}} + e^{-\frac{(\mathbf{E}_{k,\sigma} - \mu \mathbf{I}_{m_{k,\sigma}})}{k_B T}} \right)^{-1} e^{-\frac{(\mathbf{E}_{k,\sigma} - \mu \mathbf{I}_{m_{k,\sigma}})}{k_B T}} \left(\Lambda^{ij} + \frac{[\mathbf{E}_{k,\sigma}, \Lambda^{ij}]}{2k_B T} \right) \left(\mathbf{I}_{m_{k,\sigma}} + e^{-\frac{(\mathbf{E}_{k,\sigma} - \mu \mathbf{I}_{m_{k,\sigma}})}{k_B T}} \right)^{-1} \\ &= \frac{\partial f_{k,\sigma}^\mu}{\partial \epsilon_{k,\sigma}} \Lambda^{ij}, \end{aligned} \quad (\text{S12})$$

where the last line uses the definition of $\mathbf{E}_{k,\sigma} = \epsilon_{k,\sigma} \mathbf{I}_{m_{k,\sigma}}$ and $f_{k,\sigma}^\mu = (1 + e^{-(\epsilon_{k,\sigma} - \mu)/k_B T})^{-1}$ along with the fact that $[\mathbf{E}_{k,\sigma}, \Lambda^{ij}] = \epsilon_{k,\sigma} [\mathbf{I}_{m_{k,\sigma}}, \Lambda^{ij}] = 0$. Using the above relation, we have

$$\text{Tr} \left(\frac{\partial f(\mathbf{E}_{k,\sigma})}{\partial E_{k,\sigma}^{ij}} \Psi_{k,\sigma}^T(\mathbf{r}) \Psi_{k,\sigma}(\mathbf{r}) \right) = \frac{\partial f_{k,\sigma}^\mu}{\partial \epsilon_{k,\sigma}} \sum_{\alpha=1}^{m_{k,\sigma}} \sum_{\beta=1}^{m_{k,\sigma}} \Lambda_{\alpha\beta}^{ij} \psi_{k,\sigma}^{(\beta)}(\mathbf{r}) \psi_{k,\sigma}^{(\alpha)}(\mathbf{r}). \quad (\text{S13})$$

where $\Lambda_{\alpha\beta}^{ij}$ is the (α, β) -th entry of Λ^{ij} . Since $\Lambda_{\alpha\beta}^{ij} = \delta_{i\alpha} \delta_{j\beta}$, the above equation simplifies to

$$\text{Tr} \left(\frac{\partial f(\mathbf{E}_{k,\sigma})}{\partial E_{k,\sigma}^{ij}} \Psi_{k,\sigma}^T(\mathbf{r}) \Psi_{k,\sigma}(\mathbf{r}) \right) = \frac{\partial f_{k,\sigma}^\mu}{\partial \epsilon_{k,\sigma}} \psi_{k,\sigma}^{(i)}(\mathbf{r}) \psi_{k,\sigma}^{(j)}(\mathbf{r}). \quad (\text{S14})$$

Similarly,

$$\mathbf{Tr} \left(\frac{\partial f(\mathbf{E}_{k,\sigma})}{\partial E_{k,\sigma}^{ij}} \right) = \frac{\partial f_{k,\sigma}^\mu}{\partial \epsilon_{k,\sigma}} \sum_{\alpha=1}^{m_{k,\sigma}} \Lambda_{\alpha\alpha}^{ij} = \frac{\partial f_{k,\sigma}^\mu}{\partial \epsilon_{k,\sigma}} \delta_{ij}. \quad (\text{S15})$$

Finally, using Eq. S14 and S15 in Eq. S11 as well as setting $\frac{\partial \mathcal{L}}{\partial E_{k,\sigma}^{ij}}$ to zero, we get

$$\int \psi_{k,\sigma}^{(i)}(\mathbf{r}) p_{k,\sigma}^{(j)}(\mathbf{r}) d\mathbf{r} = \frac{\partial f_{k,\sigma}^\mu}{\partial \epsilon_{k,\sigma}} \left[-2 \int (\rho_\sigma^{\text{data}}(\mathbf{r}) - \rho_\sigma(\mathbf{r})) \psi_{k,\sigma}^{(i)}(\mathbf{r}) \psi_{k,\sigma}^{(j)}(\mathbf{r}) d\mathbf{r} + \eta \delta_{ij} \right]. \quad (\text{S16})$$

Thus, the above relation in matrix form can be written as

$$\int \Psi_{k,\sigma}^\mathbf{T}(\mathbf{r}) \mathbf{P}_{k,\sigma}(\mathbf{r}) d\mathbf{r} = \frac{\partial f_{k,\sigma}^\mu}{\partial \epsilon_{k,\sigma}} \left[-2 \int (\rho_\sigma^{\text{data}}(\mathbf{r}) - \rho_\sigma(\mathbf{r})) \Psi_{k,\sigma}^\mathbf{T}(\mathbf{r}) \Psi_{k,\sigma}(\mathbf{r}) d\mathbf{r} + \eta \mathbf{I}_{m_{k,\sigma}} \right]. \quad (\text{S17})$$

This concludes the derivation of Eq. 8 in the main manuscript.

C. Derivation of Eq. 9 in the main manuscript

The partial derivative of \mathcal{L} with respect to μ is given by

$$\frac{\partial \mathcal{L}}{\partial \mu} = -2 \int \sum_{\sigma} (\rho_\sigma^{\text{data}}(\mathbf{r}) - \rho_\sigma(\mathbf{r})) \sum_{k=1}^{M_\sigma} \mathbf{Tr} \left(\frac{\partial f(\mathbf{E}_{k,\sigma})}{\partial \mu} \Psi_{k,\sigma}^\mathbf{T}(\mathbf{r}) \Psi_{k,\sigma}(\mathbf{r}) \right) d\mathbf{r} + \eta \sum_{\sigma} \sum_{k=1}^{M_\sigma} \mathbf{Tr} \left(\frac{\partial f(\mathbf{E}_{k,\sigma})}{\partial \mu} \right). \quad (\text{S18})$$

Using $f(\mathbf{E}_{k,\sigma}) = f_{k,\sigma}^\mu \mathbf{I}_{m_{k,\sigma}}$ in the above and setting $\frac{\partial \mathcal{L}}{\partial \mu}$ to zero, leads to

$$\eta \sum_{\sigma} \sum_{k=1}^{M_\sigma} m_{k,\sigma} \frac{\partial f_{k,\sigma}^\mu}{\partial \mu} = 2 \sum_{\sigma} \sum_{k=1}^{M_\sigma} \frac{\partial f_{k,\sigma}^\mu}{\partial \mu} \int (\rho_\sigma^{\text{data}}(\mathbf{r}) - \rho_\sigma(\mathbf{r})) \mathbf{Tr} \left(\Psi_{k,\sigma}^\mathbf{T}(\mathbf{r}) \Psi_{k,\sigma}(\mathbf{r}) \right) d\mathbf{r}, \quad (\text{S19})$$

same as Eq. 9 in the main manuscript.

S2. UNIQUENESS OF $\delta \mathcal{L} / \delta v_{xc,\sigma}(\mathbf{r})$

To show the uniqueness of $\delta \mathcal{L} / \delta v_{xc,\sigma}(\mathbf{r})$ for a given $v_{xc,\sigma}(\mathbf{r})$, we begin with adjoint equation (Eq. 7 in the main manuscript),

$$\hat{\mathcal{H}}_\sigma(\mathbf{r}) \mathbf{P}_{k,\sigma} - \mathbf{P}_{k,\sigma}(\mathbf{r}) \mathbf{E}_{k,\sigma} = 4 (\rho_\sigma^{\text{data}}(\mathbf{r}) - \rho_\sigma(\mathbf{r})) \Psi_{k,\sigma}(\mathbf{r}) f(\mathbf{E}_{k,\sigma}) - \Psi_{k,\sigma}(\mathbf{r}) (\mathbf{D}_{k,\sigma} + \mathbf{D}_{k,\sigma}^\mathbf{T}). \quad (\text{S20})$$

Left multiplying the above equation with $\Psi_{k,\sigma}^\mathbf{T}(\mathbf{r})$ and integrating over the domain, yields

$$\mathbf{D}_{k,\sigma} + \mathbf{D}_{k,\sigma}^\mathbf{T} = 4 \left[\int \Psi_{k,\sigma}^\mathbf{T}(\mathbf{r}) (\rho_\sigma^{\text{data}}(\mathbf{r}) - \rho_\sigma(\mathbf{r})) \Psi_{k,\sigma}(\mathbf{r}) d\mathbf{r} \right] f(\mathbf{E}_{k,\sigma}), \quad (\text{S21})$$

where we have used the fact that $\Psi_{k,\sigma}$ are eigenfunctions of $\hat{\mathcal{H}}_\sigma$ (i.e., $\hat{\mathcal{H}}_\sigma \Psi_{k,\sigma} = \Psi_{k,\sigma} \mathbf{E}_{k,\sigma}$). In the case of a degenerate eigenvalue, $\Psi_{k,\sigma}$ cannot be determined uniquely. That is, given an orthogonal matrix $\mathbf{Q}_{k,\sigma}$ (i.e., $\mathbf{Q}_{k,\sigma}^\mathbf{T} \mathbf{Q}_{k,\sigma} = \mathbf{Q}_{k,\sigma} \mathbf{Q}_{k,\sigma}^\mathbf{T} = \mathbf{I}_{m_{k,\sigma}}$), $\tilde{\Psi}_{k,\sigma} = \Psi_{k,\sigma} \mathbf{Q}_{k,\sigma}$ will satisfy the KS eigenvalue problem and the orthonormality condition. Further, $\tilde{\Psi}_{k,\sigma}$ will also preserve the density ρ_σ (see Eq. 5 of the main manuscript). Denoting the corresponding $\mathbf{P}_{k,\sigma}(\mathbf{r})$ and $\mathbf{D}_{k,\sigma}$ for $\tilde{\Psi}_{k,\sigma}$ as $\tilde{\mathbf{P}}_{k,\sigma}(\mathbf{r})$ and $\tilde{\mathbf{D}}_{k,\sigma}$, respectively, Eq. S20 and Eq. S21 can be rewritten as

$$\hat{\mathcal{H}}_\sigma(\mathbf{r}) \tilde{\mathbf{P}}_{k,\sigma}(\mathbf{r}) - \tilde{\mathbf{P}}_{k,\sigma}(\mathbf{r}) \mathbf{E}_{k,\sigma} = 4 (\rho_\sigma^{\text{data}}(\mathbf{r}) - \rho_\sigma(\mathbf{r})) \tilde{\Psi}_{k,\sigma}(\mathbf{r}) f(\mathbf{E}_{k,\sigma}) - \tilde{\Psi}_{k,\sigma}(\mathbf{r}) (\tilde{\mathbf{D}}_{k,\sigma} + \tilde{\mathbf{D}}_{k,\sigma}^\mathbf{T}) \quad (\text{S22})$$

$$\tilde{\mathbf{D}}_{k,\sigma} + \tilde{\mathbf{D}}_{k,\sigma}^T = 4 \left[\int \tilde{\Psi}_{k,\sigma}^T(\mathbf{r}) (\rho_\sigma^{\text{data}}(\mathbf{r}) - \rho_\sigma(\mathbf{r})) \tilde{\Psi}_{k,\sigma}(\mathbf{r}) d\mathbf{r} \right] f(\mathbf{E}_{k,\sigma}). \quad (\text{S23})$$

Substituting $\tilde{\Psi}_{k,\sigma} = \Psi_{k,\sigma} \mathbf{Q}_{k,\sigma}$ in the above two equations leads to

$$\hat{\mathcal{H}}_\sigma(\mathbf{r}) \tilde{\mathbf{P}}_{k,\sigma} - \tilde{\mathbf{P}}_{k,\sigma}(\mathbf{r}) \mathbf{E}_{k,\sigma} = 4 (\rho_\sigma^{\text{data}}(\mathbf{r}) - \rho_\sigma(\mathbf{r})) \Psi_{k,\sigma}(\mathbf{r}) \mathbf{Q}_{k,\sigma} f(\mathbf{E}_{k,\sigma}) - \Psi_{k,\sigma}(\mathbf{r}) \mathbf{Q}_{k,\sigma} (\tilde{\mathbf{D}}_{k,\sigma} + \tilde{\mathbf{D}}_{k,\sigma}^T), \quad (\text{S24})$$

$$\tilde{\mathbf{D}}_{k,\sigma} + \tilde{\mathbf{D}}_{k,\sigma}^T = 4 \left[\int \mathbf{Q}_{k,\sigma}^T \Psi_{k,\sigma}^T(\mathbf{r}) (\rho_\sigma^{\text{data}}(\mathbf{r}) - \rho_\sigma(\mathbf{r})) \Psi_{k,\sigma}(\mathbf{r}) \mathbf{Q}_{k,\sigma} d\mathbf{r} \right] f(\mathbf{E}_{k,\sigma}). \quad (\text{S25})$$

Multiplying the above equation with $\mathbf{Q}_{k,\sigma}$ from the left yields,

$$\begin{aligned} \mathbf{Q}_{k,\sigma} (\tilde{\mathbf{D}}_{k,\sigma} + \tilde{\mathbf{D}}_{k,\sigma}^T) &= 4 \left[\int \mathbf{Q}_{k,\sigma} \mathbf{Q}_{k,\sigma}^T \Psi_{k,\sigma}^T(\mathbf{r}) (\rho_\sigma^{\text{data}}(\mathbf{r}) - \rho_\sigma(\mathbf{r})) \Psi_{k,\sigma}(\mathbf{r}) \mathbf{Q}_{k,\sigma} d\mathbf{r} \right] f(\mathbf{E}_{k,\sigma}) \\ &= (\mathbf{D}_{k,\sigma} + \mathbf{D}_{k,\sigma}^T) \mathbf{Q}_{k,\sigma}. \end{aligned} \quad (\text{S26})$$

Now, using the above relation in Eq. S24 results in

$$\hat{\mathcal{H}}_\sigma(\mathbf{r}) \tilde{\mathbf{P}}_{k,\sigma}(\mathbf{r}) - \tilde{\mathbf{P}}_{k,\sigma}(\mathbf{r}) \mathbf{E}_{k,\sigma} = 4 (\rho_\sigma^{\text{data}}(\mathbf{r}) - \rho_\sigma(\mathbf{r})) \Psi_{k,\sigma}(\mathbf{r}) \mathbf{Q}_{k,\sigma} f(\mathbf{E}_{k,\sigma}) - \Psi_{k,\sigma}(\mathbf{r}) (\mathbf{D}_{k,\sigma} + \mathbf{D}_{k,\sigma}^T) \mathbf{Q}_{k,\sigma}. \quad (\text{S27})$$

Comparing the above equation with Eq. S20, it is straightforward to note that $\tilde{\mathbf{P}}_{k,\sigma} = \mathbf{P}_{k,\sigma} \mathbf{Q}_{k,\sigma}$. That, is for an orthogonal transformation of $\Psi_{k,\sigma}$, its corresponding adjoint function is also transformed similarly. Finally, rewriting $\frac{\delta \mathcal{L}}{\delta v_{\text{xc},\sigma}(\mathbf{r})} = \sum_{k=1}^{M_\sigma} \text{Tr} \left(\mathbf{P}_{k,\sigma}^T(\mathbf{r}) \Psi_{k,\sigma}(\mathbf{r}) \right)$ (see Eq. 10 in main manuscript) in terms of $\tilde{\Psi}_{k,\sigma}$ and $\tilde{\mathbf{P}}_{k,\sigma}$, we have

$$\frac{\delta \mathcal{L}}{\delta v_{\text{xc},\sigma}(\mathbf{r})} = \sum_{k=1}^{M_\sigma} \text{Tr} \left(\tilde{\mathbf{P}}_{k,\sigma}^T(\mathbf{r}) \tilde{\Psi}_{k,\sigma}(\mathbf{r}) \right) = \sum_{k=1}^{M_\sigma} \text{Tr} \left(\mathbf{Q}_{k,\sigma}^T \mathbf{P}_{k,\sigma}^T(\mathbf{r}) \Psi_{k,\sigma}(\mathbf{r}) \mathbf{Q}_{k,\sigma} \right) \quad (\text{S28})$$

Using the fact that the trace of products of matrices is invariant with respect to cyclic permutation (i.e., $\text{Tr}(\mathbf{ABC}) = \text{Tr}(\mathbf{BCA})$), the above equation simplifies to

$$\frac{\delta \mathcal{L}}{\delta v_{\text{xc},\sigma}(\mathbf{r})} = \sum_{k=1}^{M_\sigma} \text{Tr} \left(\mathbf{P}_{k,\sigma}^T(\mathbf{r}) \Psi_{k,\sigma}(\mathbf{r}) \mathbf{Q}_{k,\sigma} \mathbf{Q}_{k,\sigma}^T \right) = \sum_{k=1}^{M_\sigma} \text{Tr} \left(\mathbf{P}_{k,\sigma}^T(\mathbf{r}) \Psi_{k,\sigma}(\mathbf{r}) \right) \quad (\text{S29})$$

This shows the uniqueness of $\delta \mathcal{L} / \delta v_{\text{xc},\sigma}(\mathbf{r})$ for a given $v_{\text{xc},\sigma}(\mathbf{r})$.

S3. SOLUTION PROCEDURE

Below we provide the overall solution procedure to solve the inverse DFT problem for a given spin densities ($\rho_\sigma^{\text{data}}(\mathbf{r})$).

1. For the current iterate of $v_{\text{xc},\sigma}(\mathbf{r})$, solve the KS eigenvalue problem (Eq. 2 in the main manuscript) to find $\Psi_{k,\sigma}(\mathbf{r})$ and $\mathbf{E}_{k,\sigma}$. Subsequently, evaluate $\rho_\sigma(\mathbf{r})$ (Eq. 4 in the main manuscript) and μ (Eq. 5 in the main manuscript).
2. Using $\Psi_{k,\sigma}$, $\mathbf{E}_{k,\sigma}$ and μ , solve for η (Eq. 9 in the main manuscript)
3. Using $\Psi_{k,\sigma}$, $\mathbf{E}_{k,\sigma}$, μ , and η , solve for the overlap between the KS orbitals and their adjoint functions (Eq. 8 in the main manuscript)
4. Using Eq. S21, evaluate $\mathbf{D}_{k,\sigma} + \mathbf{D}_{k,\sigma}^T$ and substitute it in the adjoint equation (Eq. 7 in the main manuscript).
5. Solve the adjoint equation (Eq. 7 in the main manuscript) to find the adjoint functions ($\mathbf{P}_{k,\sigma}$). Note that the adjoint equation, by itself, does not provide a unique solution for $\mathbf{P}_{k,\sigma}$. That is, if $\mathbf{P}_{k,\sigma}$ is a solution to the adjoint equation, it can be trivially shown that for any $m_{k,\sigma} \times m_{k,\sigma}$ matrix \mathbf{A} , $\mathbf{P}_{k,\sigma} + \Psi_{k,\sigma} \mathbf{A}$ is also a solution. This is owing to the fact that $\Psi_{k,\sigma}$ are the eigenfunctions of $\hat{\mathcal{H}}_\sigma$. Nevertheless, we have an additional

condition (Eq. 8 in the main manuscript) that provides the overlap between the KS orbitals and their adjoint functions, and hence, uniquely determines the $\mathbf{P}_{k,\sigma}$. To do so, we first solve the adjoint equation in a space orthogonal to $\Psi_{k,\sigma}$ to find $\mathbf{P}_{k,\sigma}^\perp$ that is orthogonal to $\Psi_{k,\sigma}$. Subsequently, we find $\mathbf{P}_{k,\sigma} = \mathbf{P}_{k,\sigma}^\perp + \Psi_{k,\sigma}\mathbf{B}$, where $\mathbf{B} = \frac{\partial f_{k,\sigma}^\mu}{\partial \epsilon_{k,\sigma}} \left[-2 \int (\rho_\sigma^{\text{data}}(\mathbf{r}) - \rho_\sigma(\mathbf{r})) \Psi_{k,\sigma}^\text{T}(\mathbf{r}) \Psi_{k,\sigma}(\mathbf{r}) d\mathbf{r} + \eta \mathbf{I}_{m_{k,\sigma}} \right]$ (i.e., the right hand side of Eq. 8 in the main manuscript).

6. Update $v_{xc,\sigma}(\mathbf{r})$ using Eq. 10 in the main manuscript
7. Go to step 1 and repeat until convergence in ρ_σ (i.e., $\|\rho_\sigma^{\text{data}} - \rho_\sigma\|$ is below a tolerance).

S4. NON-INTERACTING ENSEMBLE-V-REPRESENTABLE DENSITY

The KS density matrix ($\hat{\mathcal{D}}_\sigma$), in general, can be non-interacting ensemble-v-representable (e- v_s) as it can be expressed as an ensemble of L degenerate KS Slater determinants,

$$\hat{\mathcal{D}}_\sigma = \sum_{j=1}^L d_j |\Phi_{j,\sigma}\rangle \langle \Phi_{j,\sigma}|, \quad d_j \geq 0, \quad \sum_{j=1}^L d_j = 1. \quad (\text{S30})$$

In the above equation, $\{|\Phi_{j,\sigma}\rangle\}$ denote the L degenerate KS determinants. The corresponding density is given by,

$$\rho_\sigma(\mathbf{r}) = \text{Tr} \left(\hat{\mathcal{D}}_\sigma \hat{\rho}_\sigma(\mathbf{r}) \right) = \sum_{j=1}^L d_j \rho_{j,\sigma}(\mathbf{r}), \quad (\text{S31})$$

where $\hat{\rho}_\sigma$ is the density operator and $\rho_{j,\sigma}(\mathbf{r})$ is the density corresponding to $\Phi_{j,\sigma}$. The non-interacting pure- v_s representable (pure- v_s) density is a special case with $L = 1$. Typically, for an e- v_s density, the different KS Slater determinants ($\Phi_{j,\sigma}$) differ only in their highest occupied molecular orbital (HOMO), all of which are degenerate with their KS eigenvalues equal to the Fermi level (chemical potential). In other words, a typical e- v_s density can be written as

$$\rho_\sigma(\mathbf{r}) = \sum_{i:\epsilon_{i,\sigma} < \mu} |\psi_{i,\sigma}(\mathbf{r})|^2 + \sum_{i:\epsilon_{i,\sigma} = \mu} f |\psi_{i,\sigma}(\mathbf{r})|^2, \quad (\text{S32})$$

where f is the fractional occupancy of the HOMO level (typically equal to $1/L$).

For a given density, it is *a priori* difficult to ascertain if it is a pure- v_s or an e- v_s density. However, any robust approach to the inverse DFT problem should be flexible enough to admit both kinds of densities. All the densities for the benchmark systems considered (Li, C, N, O, CN, and CH₂) turn out to be pure- v_s . In this example, we demonstrate the efficacy of the proposed inverse DFT approach for e- v_s density by using the SCAN0 based density for boron (B), obtained using a finite temperature Fermi-Dirac smearing in the groundstate calculation. Upon inversion, we obtain an ensemble of three KS Slater determinants for the majority-spin. To elaborate, we obtain three degenerate KS orbitals at the Fermi level (μ). The density for the minority-spin turns out to be pure- v_s . Fig. S1 presents the SCAN0 based XC potentials for B.

S5. ERRORS IN MODEL DENSITIES AND POTENTIALS

We report the error in the densities obtained from self-consistently solved calculations with approximate XC functionals (denoted as $\rho_{\sigma,\text{model}}^{\text{data}}$), relative to the ground-state density from heat-bath configuration interaction (HBCI) calculations (denoted as $\rho_{\sigma,\text{exact}}^{\text{data}}$). We quantify the errors in the density using two metrics

$$f_{1,\sigma} = \frac{\|\rho_{\sigma,\text{exact}}^{\text{data}} - \rho_{\sigma,\text{model}}^{\text{data}}\|_{L_2}}{\|\rho_{\sigma,\text{exact}}^{\text{data}}\|_{L_2}}, \quad f_{2,\sigma} = \frac{\|\|\nabla(\rho_{\sigma,\text{exact}}^{\text{data}} - \rho_{\sigma,\text{model}}^{\text{data}})\|\|_{L_2}}{\|\|\nabla\rho_{\sigma,\text{exact}}^{\text{data}}\|\|_{L_2}}. \quad (\text{S33})$$

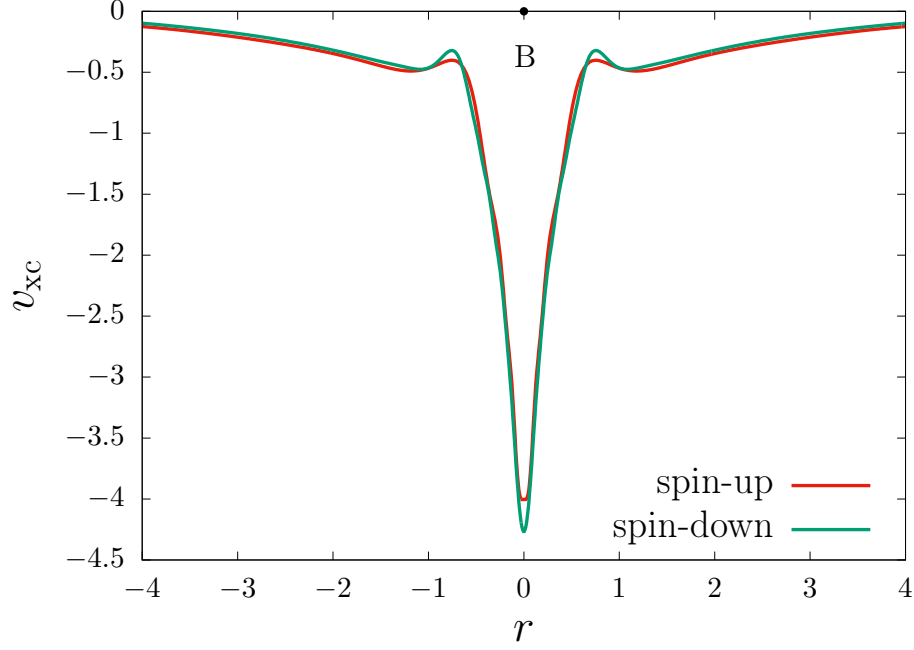


FIG. S1. SCAN0 based XC potentials for B. The majority-spin density is an $e-v_s$ density.

TABLE I. Comparing the exact and the model density in terms of $f_{1,\sigma}$ and $f_{2,\sigma}$ values (Eq. S33) for the majority-spin.

Model	Li		C		N		O		CN		CH ₂	
	f_1	f_2	f_1	f_2	f_1	f_2	f_1	f_2	f_1	f_2	f_1	f_2
B3LYP	0.007	0.013	0.004	0.006	0.004	0.005	0.003	0.004	0.003	0.005	0.004	0.005
SCAN0	0.003	0.006	0.003	0.003	0.002	0.002	0.002	0.002	0.005	0.003	0.003	0.003
SCAN	0.004	0.008	0.004	0.004	0.003	0.003	0.002	0.002	0.002	0.003	0.003	0.004
PBE	0.007	0.011	0.004	0.006	0.004	0.005	0.003	0.004	0.004	0.006	0.014	0.015
PW92	0.021	0.022	0.012	0.013	0.012	0.013	0.01	0.012	0.012	0.013	0.014	0.015

We also report two additional error metric for the model XC potentials, given by

$$e_{3,\sigma} = \frac{\|\delta v_{xc,\sigma}\|_{L_2}}{\|v_{xc,\sigma}^{\text{exact}}\|_{L_2}}, \quad e_{4,\sigma} = \frac{\|\|\nabla \delta v_{xc,\sigma}\|\|_{L_2}}{\|\|\nabla v_{xc,\sigma}^{\text{exact}}\|\|_{L_2}}, \quad (\text{S34})$$

where $\delta v_{xc,\sigma} = v_{xc,\sigma}^{\text{exact}} - v_{xc,\sigma}^{\text{model}}$. We note that while $e_{1,\sigma}$ and $e_{2,\sigma}$ (presented in the main manuscript) are $\rho_\sigma^{\text{data}}$ -weighted error metrics, $e_{3,\sigma}$ and $e_{4,\sigma}$ are their unweighted counterparts, respectively.

Tables I and II list the f_1 and f_2 values for the majority- and minority-spin, for all the benchmark systems considered in this study. Table III lists the $e_{1,\sigma}$ and $e_{2,\sigma}$ errors (defined in Eq.12 of the main manuscript) for the minority-spin. Finally, Tables IV and V list the $e_{3,\sigma}$ and $e_{4,\sigma}$ errors for the majority- and minority-spin, respectively.

Comparing Tables I and II with Table I from the main manuscript (and Tables III, IV, and V here), it is evident that while the relative errors in the density are of $\mathcal{O}(10^{-3} - 10^{-2})$, the relative errors in the XC potentials are two-orders higher (i.e., $\mathcal{O}(10^{-1} - 10^0)$). This establishes the XC potential to be a quantity of greater sensitivity than the density, and hence, can be instrumental in development of future XC functionals.

TABLE II. Comparing the exact and the model density in terms of $f_{1,\sigma}$ and $f_{2,\sigma}$ values (Eq. S33) for the minority-spin.

Model	Li		C		N		O		CN		CH ₂	
	f_1	f_2	f_1	f_2	f_1	f_2	f_1	f_2	f_1	f_2	f_1	f_2
B3LYP	0.007	0.011	0.003	0.006	0.003	0.005	0.003	0.004	0.003	0.005	0.003	0.005
SCAN0	0.003	0.005	0.002	0.003	0.002	0.003	0.002	0.002	0.006	0.003	0.002	0.002
SCAN	0.004	0.008	0.003	0.004	0.002	0.003	0.002	0.002	0.003	0.003	0.003	0.003
PBE	0.007	0.012	0.004	0.007	0.003	0.006	0.003	0.005	0.004	0.006	0.012	0.013
PW92	0.021	0.022	0.011	0.012	0.01	0.011	0.009	0.01	0.012	0.013	0.012	0.013

TABLE III. Comparison of the model XC potentials in terms of the error metrics $e_{1,\sigma}$ and $e_{2,\sigma}$ (defined in Eq.12 of the main manuscript), for the minority-spin. See the main manuscript for the error metrics for majority-spin.

Model	Li		C		N		O		CN		CH ₂	
	$e_{1,\sigma}$	$e_{2,\sigma}$	$e_{1,\sigma}$	$e_{2,\sigma}$	$e_{1,\sigma}$	$e_{2,\sigma}$	$e_{1,\sigma}$	$e_{2,\sigma}$	$e_{1,\sigma}$	$e_{2,\sigma}$	$e_{1,\sigma}$	$e_{2,\sigma}$
B3LYP	0.097	1.841	0.105	1.511	0.102	1.292	0.104	1.391	0.107	1.511	0.109	1.717
SCAN0	0.045	0.499	0.053	0.324	0.05	0.409	0.045	0.427	0.05	0.372	0.047	0.417
SCAN	0.064	0.853	0.053	0.483	0.057	0.56	0.052	0.575	0.052	0.499	0.053	0.563
PBE	0.107	2.169	0.116	1.755	0.115	1.478	0.118	1.579	0.12	1.739	0.118	1.744
PW92	0.105	0.323	0.116	0.514	0.11	0.565	0.112	0.604	0.107	0.64	0.105	0.658

S6. COMPARISON OF KOHN-SHAM EIGENVALUES

In this section, we compare the Kohn-Sham eigenvalues corresponding to the exact and the model XC potentials. Tables VI– XI compares the Kohn-Sham eigenvalues for Li, C, N, O, CN, and CH₂, respectively. For each system, we provide the error in the eigenvalues of a model XC, defined as

$$\Delta\epsilon_{\sigma}^{\text{model}} = \frac{1}{N_{\sigma}} \sum_i^{N_{\sigma}} |\epsilon_{i,\sigma}^{\text{exact}} - (\epsilon_{i,\sigma}^{\text{model}} + \Delta\mu^{\text{model}})|, \quad (\text{S35})$$

where $\epsilon_{i,\sigma}^{\text{exact}}$ and $\epsilon_{i,\sigma}^{\text{model}}$ are the i^{th} Kohn-Sham eigenvalue for spin-index σ corresponding to the exact and model XC potentials, respectively; and $\Delta\mu^{\text{model}} = \mu^{\text{exact}} - \mu^{\text{model}}$ is the difference between the chemical potential (see Eq. 5 in main manuscript) for the Kohn-Sham systems corresponding to the exact and model XC potentials. The $\Delta\mu^{\text{model}}$ helps to remove any constant shift in the eigenvalues.

TABLE IV. Comparison of the model XC potentials in terms of the error metrics $e_{3,\sigma}$ and $e_{4,\sigma}$ (defined in Eq. S34) for the majority-spin.

Model	Li		C		N		O		CN		CH ₂	
	$e_{3,\sigma}$	$e_{4,\sigma}$	$e_{3,\sigma}$	$e_{4,\sigma}$	$e_{3,\sigma}$	$e_{4,\sigma}$	$e_{3,\sigma}$	$e_{4,\sigma}$	$e_{3,\sigma}$	$e_{4,\sigma}$	$e_{3,\sigma}$	$e_{4,\sigma}$
B3LYP	0.759	0.665	0.789	0.442	0.788	0.413	0.783	0.391	0.772	0.37	0.781	0.478
SCAN0	0.714	0.65	0.742	0.364	0.738	0.318	0.733	0.304	0.727	0.284	0.733	0.373
SCAN	0.915	0.675	0.918	0.311	0.929	0.286	0.928	0.312	0.912	0.318	0.917	0.367
PBE	1.034	1.15	0.933	0.542	0.943	0.55	0.93	0.496	0.911	0.477	0.929	0.578
PW92	0.914	0.674	0.917	0.396	0.929	0.391	0.929	0.418	0.911	0.405	0.917	0.462

TABLE V. Comparison of the model XC potentials in terms of the error metrics $e_{3,\sigma}$ and $e_{4,\sigma}$ (defined in Eq. S34) for the minority-spin.

Model	Li		C		N		O		CN		CH ₂	
	$e_{3,\sigma}$	$e_{4,\sigma}$	$e_{3,\sigma}$	$e_{4,\sigma}$	$e_{3,\sigma}$	$e_{4,\sigma}$	$e_{3,\sigma}$	$e_{4,\sigma}$	$e_{3,\sigma}$	$e_{4,\sigma}$	$e_{3,\sigma}$	$e_{4,\sigma}$
B3LYP	0.113	1.858	0.137	1.732	0.127	1.321	0.109	1.385	0.109	1.529	0.117	1.649
SCAN0	0.077	0.513	0.1	0.419	0.086	0.326	0.064	0.382	0.055	0.37	0.072	0.435
SCAN	0.086	0.917	0.091	0.585	0.082	0.44	0.064	0.518	0.053	0.488	0.064	0.585
PBE	0.13	2.485	0.14	1.946	0.134	1.54	0.121	1.6	0.12	1.735	0.121	1.772
PW92	0.154	0.629	0.172	0.684	0.17	0.608	0.134	0.628	0.113	0.643	0.131	0.667

TABLE VI. Comparison of Kohn-Sham eigenvalues corresponding to the exact and model XC potentials for Li. σ_1 and σ_2 denote majority and minority spins, respectively. All values in a.u.

σ_1				σ_2			
Exact	B3LYP	SCAN0	SCAN	Exact	B3LYP	SCAN0	SCAN
-1.986	-1.931	-1.916	-1.896	-2.084	-1.899	-1.932	-1.925
-0.129	-0.117	-0.109	-0.117				
$\Delta\epsilon_{\sigma_1}^{\text{model}}$	0.021	0.025	0.039	$\Delta\epsilon_{\sigma_2}^{\text{model}}$	0.173	0.131	0.147

TABLE VII. Comparison of Kohn-Sham eigenvalues corresponding to the exact and model XC potentials for C. σ_1 and σ_2 denote majority and minority spins, respectively. The degenerate ones are marked with their multiplicity in parenthesis. All values in a.u.

σ_1				σ_2			
Exact	B3LYP	SCAN0	SCAN	Exact	B3LYP	SCAN0	SCAN
-10.204	-9.983	-10.010	-10.070	-10.462	-9.962	-10.007	-10.051
-0.675	-0.463	-0.489	-0.539	-0.584	-0.360	-0.377	-0.442
-0.361 (2)	-0.160 (2)	-0.186 (2)	-0.238 (2)				
$\Delta\epsilon_{\sigma_1}^{\text{model}}$	0.008	0.008	0.006	$\Delta\epsilon_{\sigma_2}^{\text{model}}$	0.161	0.156	0.154

TABLE VIII. Comparison of Kohn-Sham eigenvalues corresponding to the exact and model XC potentials for N. σ_1 and σ_2 denote majority and minority spins, respectively. The degenerate ones are marked with their multiplicity in parenthesis. All values in a.u.

σ_1				σ_2			
Exact	B3LYP	SCAN0	SCAN	Exact	B3LYP	SCAN0	SCAN
-14.251	-14.056	-14.084	-14.164	-14.566	-14.032	-14.100	-14.129
-0.887	-0.667	-0.695	-0.750	-0.720	-0.505	-0.508	-0.565
-0.452 (3)	-0.243 (3)	-0.264 (3)	-0.322 (3)				
$\Delta\epsilon_{\sigma_1}^{\text{model}}$	0.005	0.005	0.010	$\Delta\epsilon_{\sigma_2}^{\text{model}}$	0.165	0.150	0.165

TABLE IX. Comparison of Kohn-Sham eigenvalues corresponding to the exact and model XC potentials for O. σ_1 and σ_2 denote majority and minority spins, respectively. The degenerate ones are marked with their multiplicity in parenthesis. All values in a.u.

σ_1				σ_2			
Exact	B3LYP	SCAN0	SCAN	Exact	B3LYP	SCAN0	SCAN
-19.069	-18.849	-18.891	-18.951	-19.181	-18.805	-18.831	-18.871
-1.097	-0.866	-0.913	-0.953	-0.951	-0.719	-0.738	-0.787
-0.560 (2)	-0.340 (2)	-0.381 (2)	-0.425 (2)	-0.438	-0.208	-0.240	-0.290
-0.488	-0.269	-0.301	-0.344				
$\Delta\epsilon_{\sigma_1}^{\text{model}}$	0.025	0.021	0.058	$\Delta\epsilon_{\sigma_2}^{\text{model}}$	0.073	0.076	0.081

TABLE X. Comparison of Kohn-Sham eigenvalues corresponding to the exact and model XC potentials for CN. σ_1 and σ_2 denote majority and minority spins, respectively. The degenerate ones are marked with their multiplicity in parenthesis. All values in a.u.

σ_1				σ_2			
Exact	B3LYP	SCAN0	SCAN	Exact	B3LYP	SCAN0	SCAN
-14.197	-13.970	-13.948	-14.025	-14.216	-13.959	-13.947	-14.024
-10.143	-9.935	-9.933	-9.997	-10.183	-9.914	-9.914	-9.989
-0.975	-0.810	-0.833	-0.894	-0.969	-0.783	-0.813	-0.877
-0.549	-0.376	-0.408	-0.468	-0.512	-0.323	-0.345	-0.411
-0.452	-0.289	-0.309	-0.375	-0.447 (2)	-0.269 (2)	-0.295 (2)	-0.361 (2)
-0.448 (2)	-0.281 (2)	-0.300 (2)	-0.364 (2)				
$\Delta\epsilon_{\sigma_1}^{\text{model}}$	0.019	0.027	0.024	$\Delta\epsilon_{\sigma_2}^{\text{model}}$	0.031	0.042	0.040

TABLE XI. Comparison of Kohn-Sham eigenvalues corresponding to the exact and model XC potentials for CH₂. σ_1 and σ_2 denote majority and minority spins, respectively. All values in a.u.

σ_1				σ_2			
Exact	B3LYP	SCAN0	SCAN	Exact	B3LYP	SCAN0	SCAN
-10.067	-9.894	-9.922	-9.988	-10.174	-9.859	-9.886	-9.949
-0.718	-0.547	-0.575	-0.627	-0.682	-0.476	-0.501	-0.566
-0.476	-0.310	-0.328	-0.382	-0.481	-0.276	-0.305	-0.371
-0.380	-0.210	-0.240	-0.293				
-0.310	-0.144	-0.175	-0.229				
$\Delta\epsilon_{\sigma_1}^{\text{model}}$	0.003	0.007	0.006	$\Delta\epsilon_{\sigma_2}^{\text{model}}$	0.075	0.080	0.068

S7. EXACT AND MODEL XC POTENTIALS

In this section, we present a comparison of the exact and model XC potentials for Li and N atom. Figures S2 and S3 provide the comparison for Li and N, respectively. Additionally, Figs. S4- S6 present the comparison for the minority-spin for C, O, and CN, respectively (see the main manuscript for the comparison of the majority-spin). Figures S7 and S8 provide the exact and model XC potentials for the CH₂ molecule on the plane of the molecule, for the both the spins. For CH₂, we also provide the error in model XC potentials, for both the spins, in Fig. S9 and Fig. S10. As evident, the model XC potentials differ significantly from the exact ones. In all cases, SCAN0 and SCAN provide better qualitative and quantitative agreement, including the presence of atomic inter-shell structure. Note the minority-spin of Li has no atomic intershell structure, which is expected, as the density is composed of a single KS orbital.

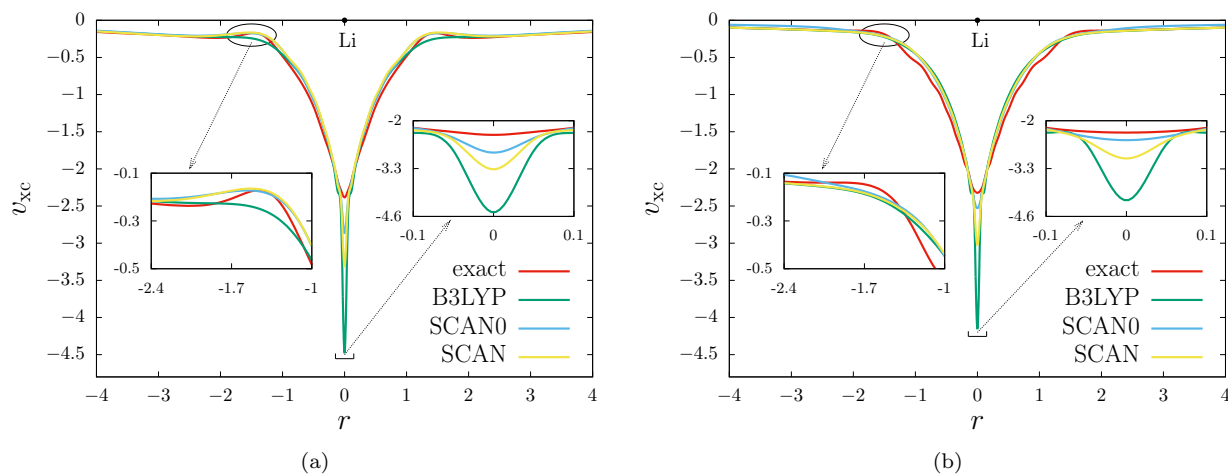


FIG. S2. Comparison of the exact and model XC potentials for Li along the dominant principal axis of the moment of inertia tensor of its density: (a) majority-spin, and (b) minority-spin.

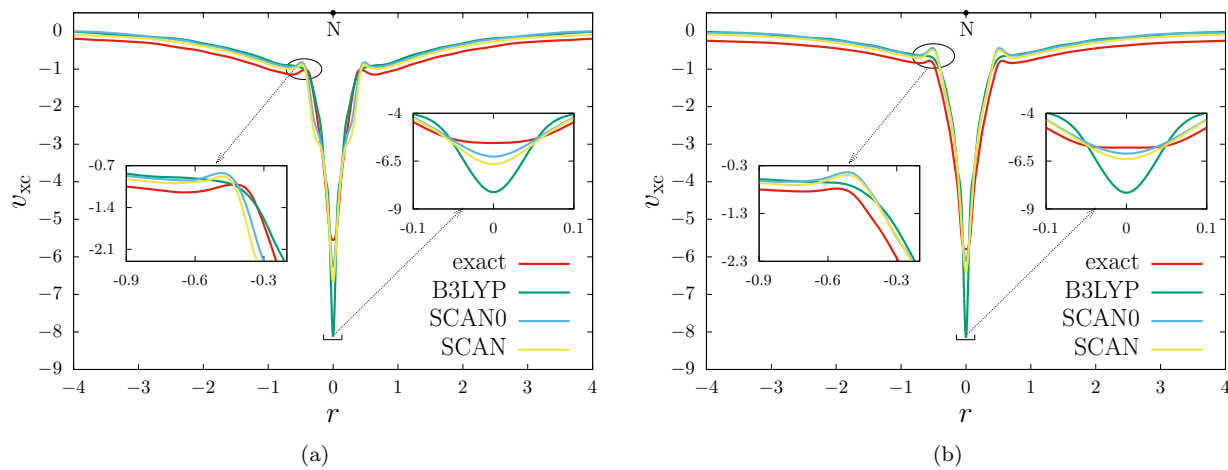


FIG. S3. Comparison of the exact and model XC potentials for N along the dominant principal axis of the moment of inertia tensor of its density: (a) majority-spin, and (b) minority-spin.

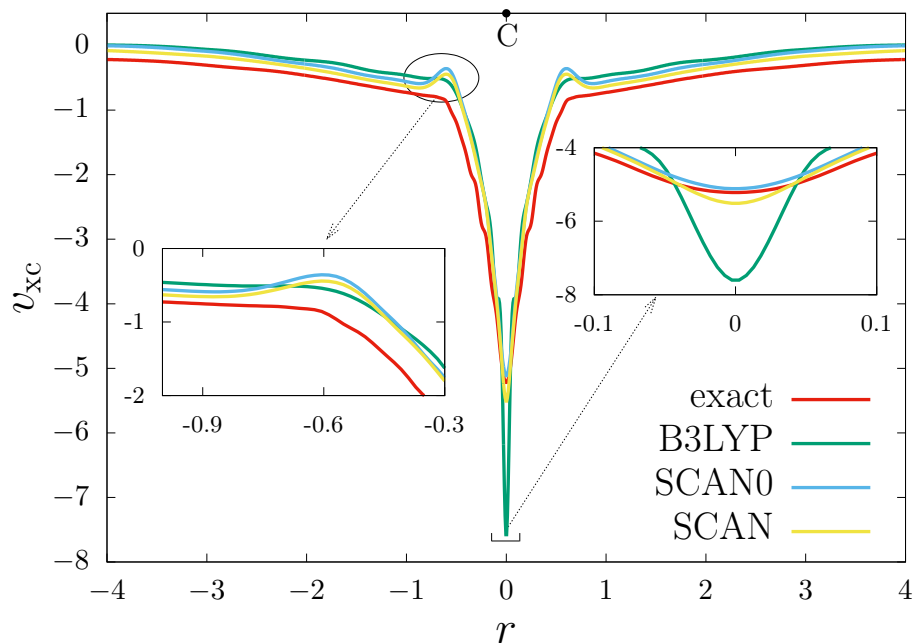


FIG. S4. Comparison of the exact and model XC potentials for C for the minority-spin, along the dominant principal axis of the moment of inertia tensor of its density.

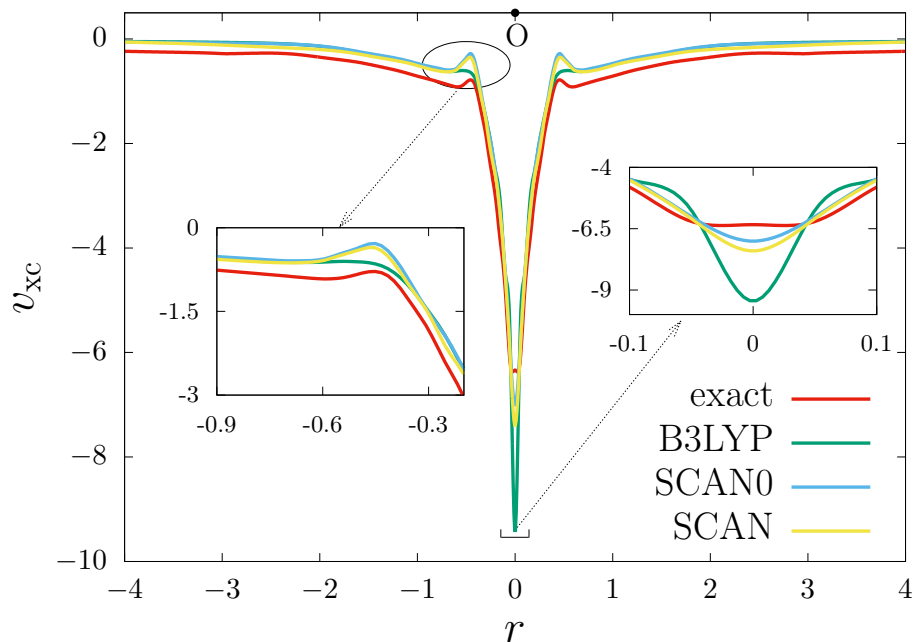


FIG. S5. Comparison of the exact and model XC potentials for O for the minority-spin, along the dominant principal axis of the moment of inertia tensor of its density.

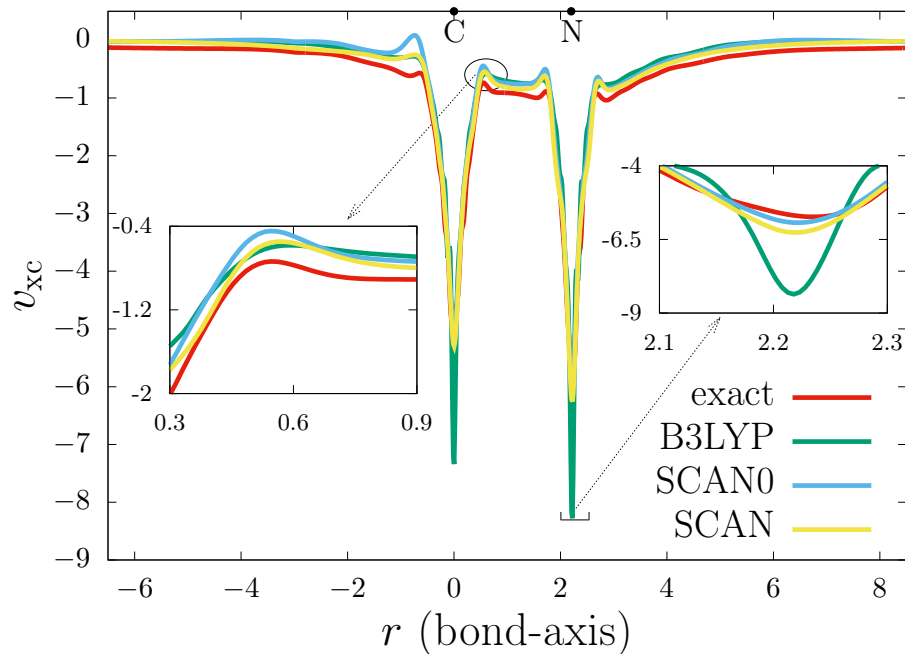


FIG. S6. Comparison of the exact and model XC potentials for CN for the minority-spin, along the bond-length.

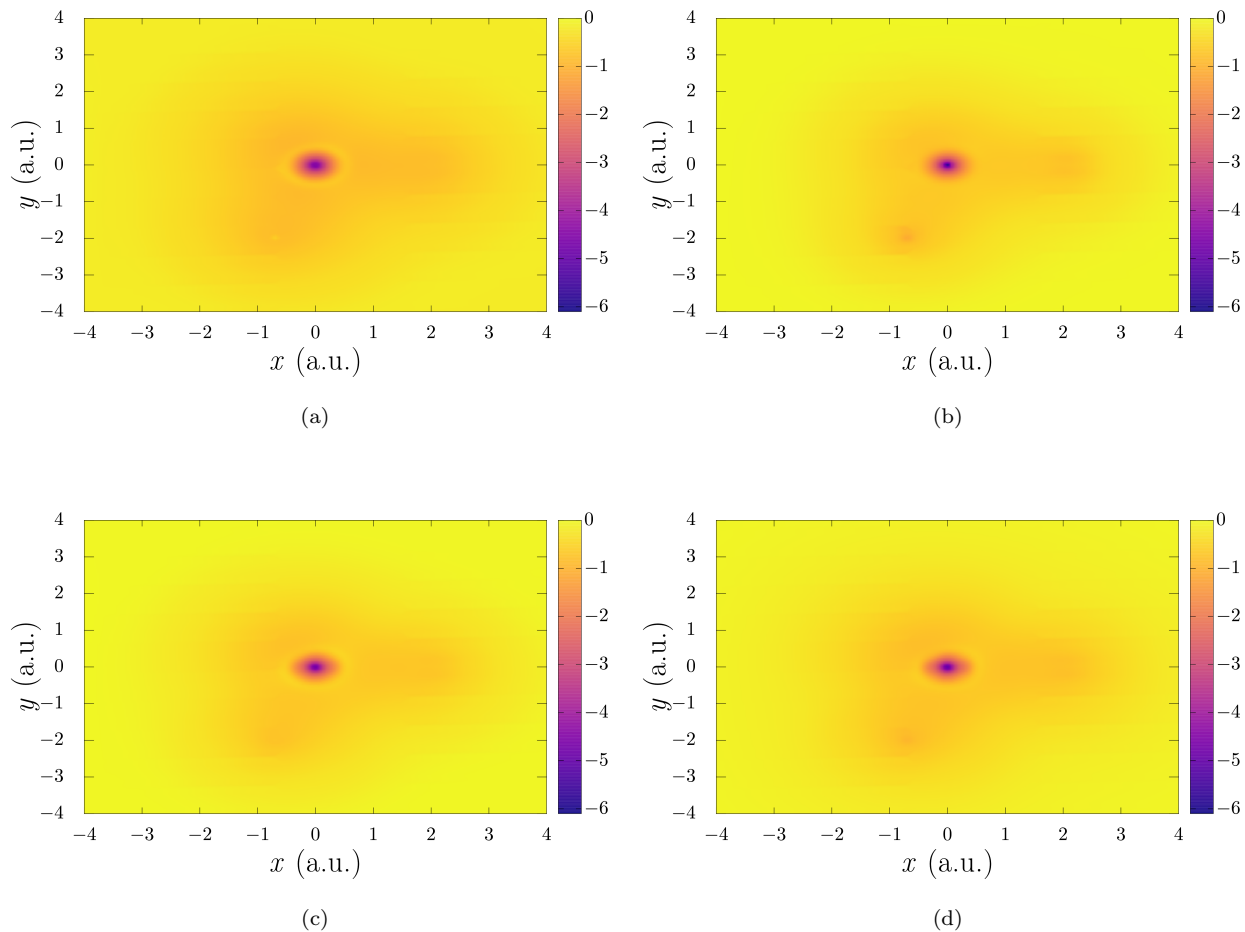


FIG. S7. Exact and model XC potentials for CH₂ on the plane of the molecule for the majority-spin: (a) exact potential, (b) B3LYP based model potential, (c) SCAN0 based model potential, and (d) SCAN based model potential. The yellow ring around the C atom in the exact, SCAN0, and SCAN potentials represent the atomic intershell structure, otherwise absent in the B3LYP based potential.

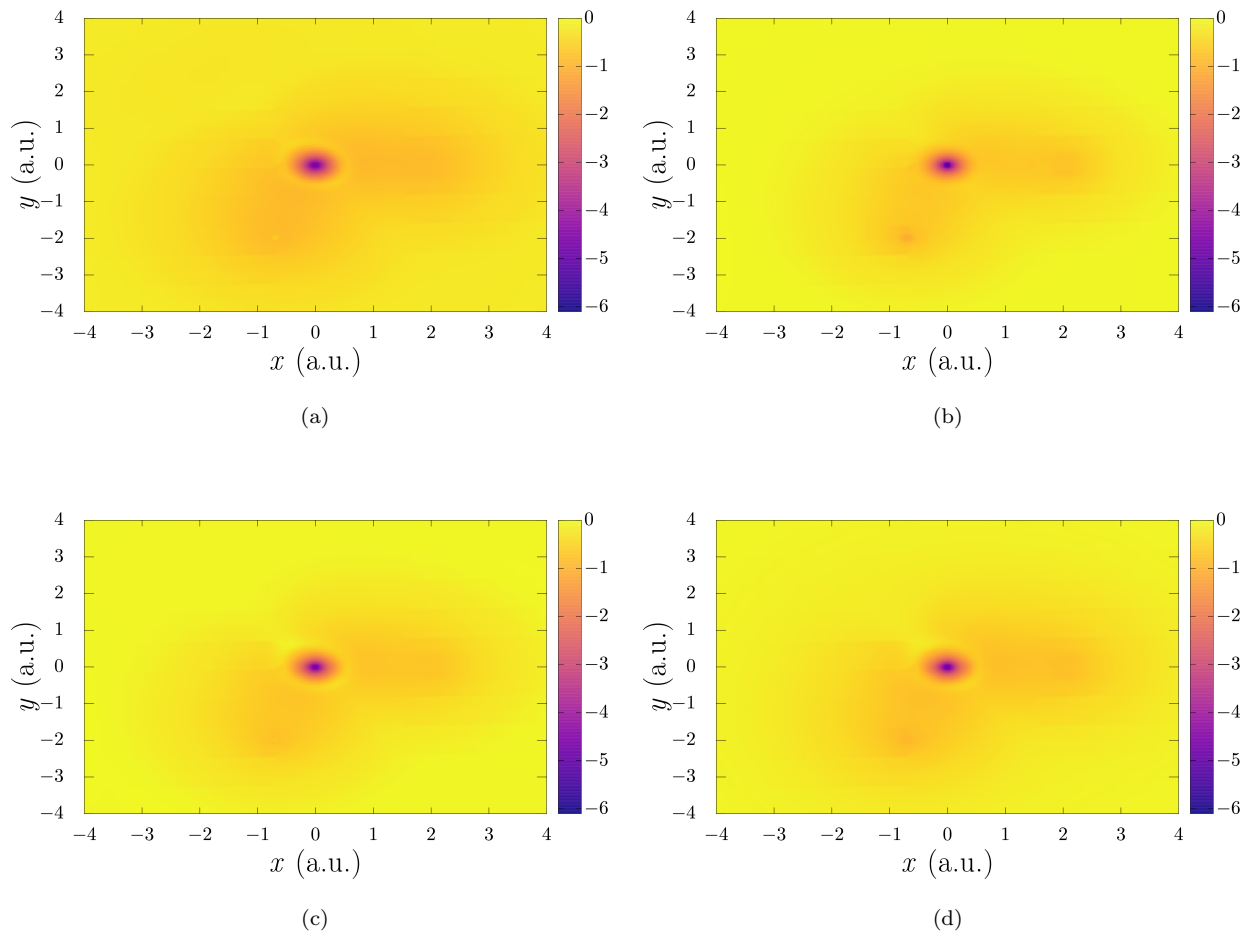


FIG. S8. Exact and model XC potentials for CH₂ on the plane of the molecule for the minority-spin: (a) exact, (b) B3LYP based model potential, (c) SCAN0 based model potential, and (d) SCAN based model potential. The yellow ring around the C atom in the exact, SCAN0, and SCAN potentials represent the atomic intershell structure, otherwise absent in the B3LYP based potential.

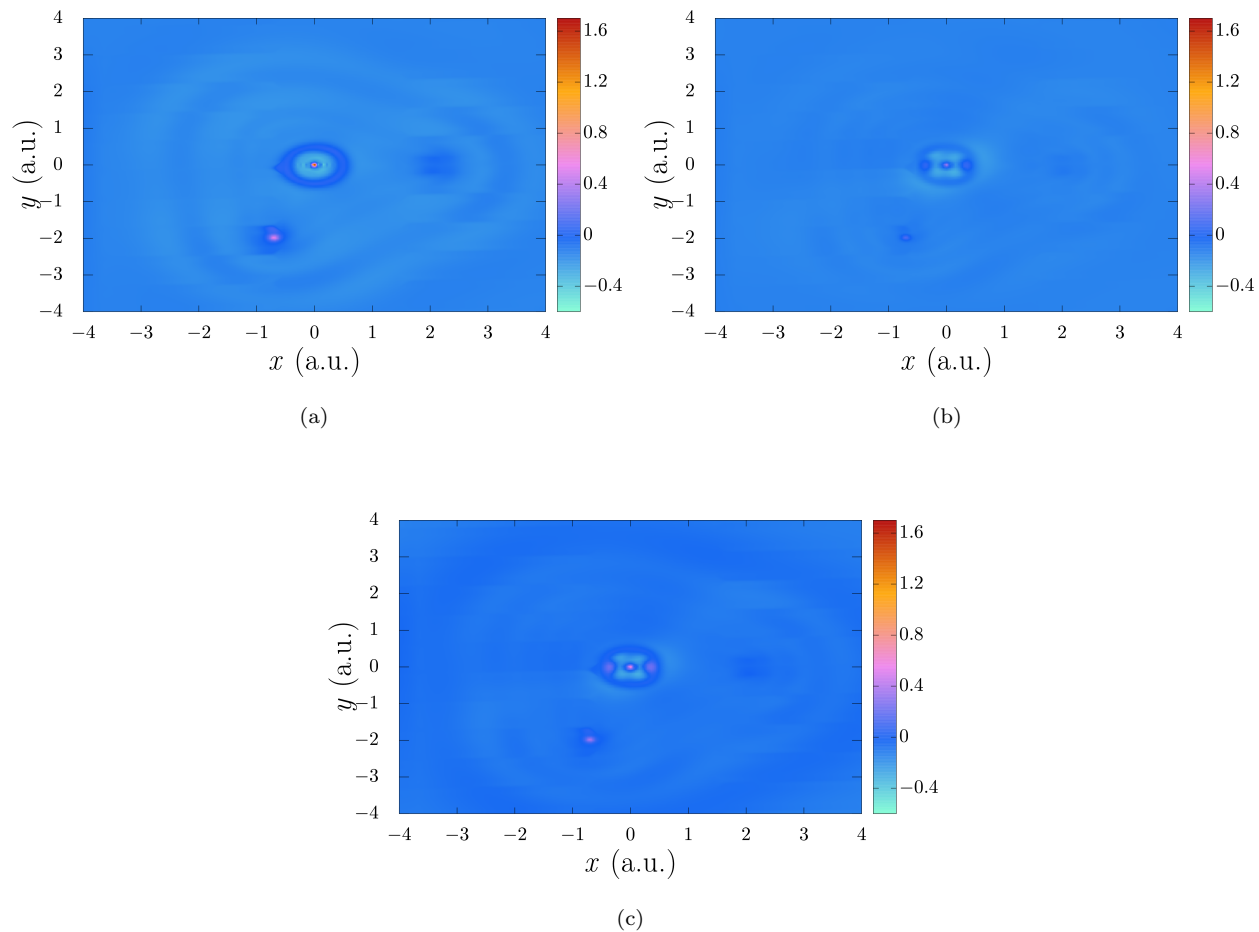


FIG. S9. Error in the model XC potentials (i.e., $v_{xc,\sigma}^{\text{exact}} - v_{xc,\sigma}^{\text{model}}$) for CH_2 on the plane of the molecule for the majority-spin: (a) B3LYP based model potential, (b) SCAN0 based model potential, and (c) SCAN based model potential.

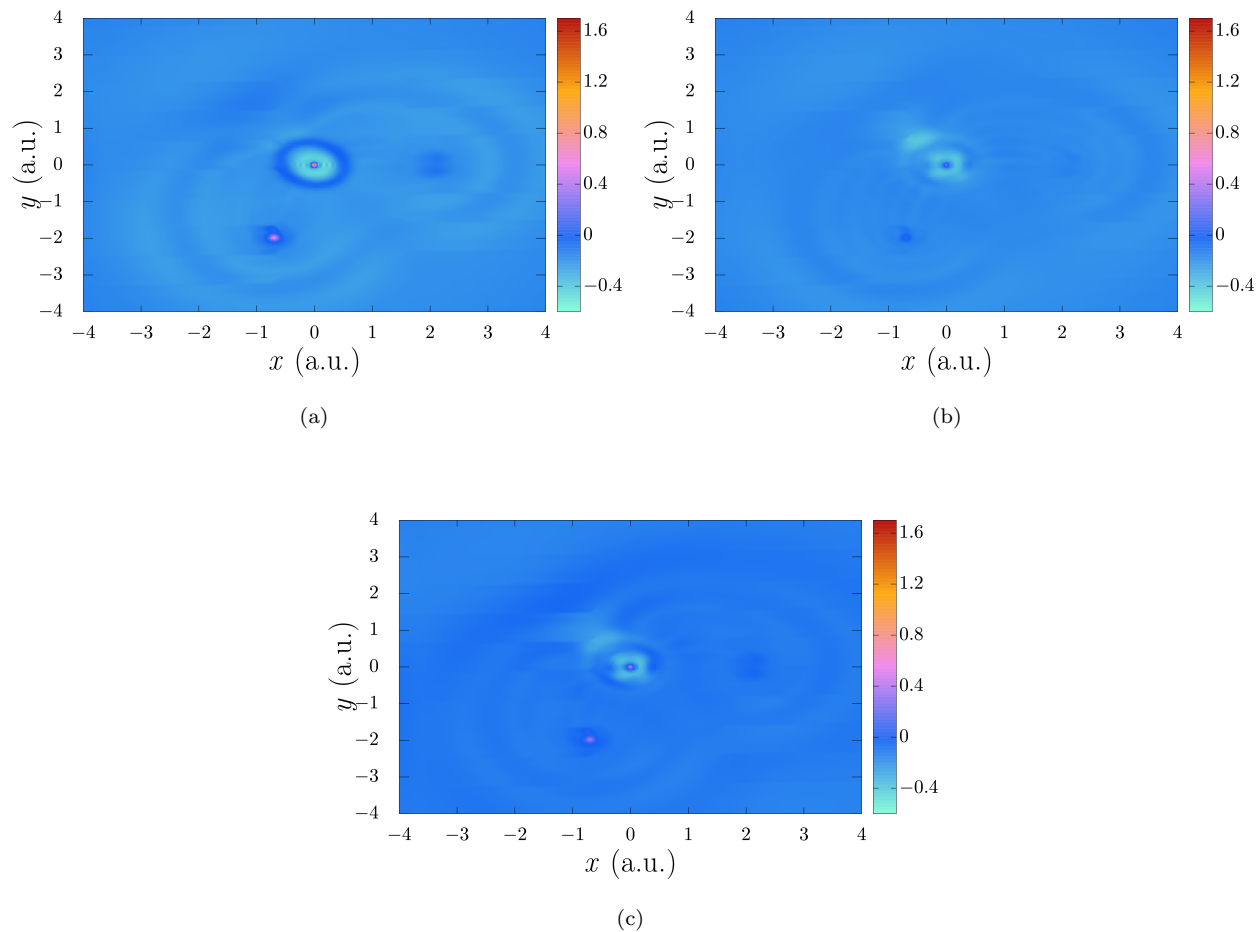


FIG. S10. Error in the model XC potentials (i.e., $v_{xc,\sigma}^{\text{exact}} - v_{xc,\sigma}^{\text{model}}$) for CH₂ on the plane of the molecule for the minority-spin: (a) B3LYP based model potential, (b) SCAN0 based model potential, and (c) SCAN based model potential.

S8. WAVEFUNCTION ENERGIES AND DENSITY MATRICES

Heat bath configuration interaction [S2–S10] (HBCI) was used to generate densities and provide total energies, as implemented in a development version of the QChem software package. [S11] HBCI begins from a reference state and systematically expands the wavefunction towards the full CI (FCI) limit. Although many implementations of HBCI start from a single-determinant reference, our implementation uses a complete active space (CAS) reference, up to a CAS (8e,8o) space. [S12, S13] HBCI consists of two steps: a variational step and a perturbative step. In the variational step, determinants from the FCI space are added if they are highly coupled to a determinant already in the space with the variational wavefunction. The latter is expressed as

$$|\psi_0\rangle = \sum_i c_i |D_i\rangle \quad (\text{S36})$$

where $|D_i\rangle$ represent the important determinants. An Epstein-Nesbet perturbation correction is then applied to the remaining determinants, using a tight threshold to determine the importance of each coupling element with the perturbative wavefunction. The perturbative component of the wavefunction is expressed as

$$|\psi_1\rangle = \sum_k \frac{\sum_i H_{ki} c_i}{E_{var} - H_{kk}} |D_k\rangle \quad (\text{S37})$$

where k enumerates the determinants not present in the variational wavefunction. New determinants are added using the following selection criteria

$$\max(|H_{ki} c_i|) > \epsilon_1 \quad (\text{S38})$$

where the parameter ϵ_1 controls the addition of new determinants. A similar parameter ϵ_2 controls the perturbative importance criteria and is naturally smaller in magnitude. The energies were converged using HBCI to tight tolerances of ϵ_1 and ϵ_2 , (see Table XII) showing a close approach to the full CI limit.

Correlation from core electrons can significantly contribute to the total correlation energy of atoms and molecules. To provide high accuracy input to inverse DFT, the core electrons were included in the CI space for all species. The core-valence polarized, quadruple zeta basis set, cc-pCVQZ, [S14, S15] was therefore applied to all systems.

All the information needed to calculate the electron density at a given point in space can be found in the one particle density matrix and the one particle, atomic orbital basis set. In closed shell systems, these density matrices are identical for α and β electrons. For open-shell systems, the α and β density matrices must be generated separately. These density matrices are generated in the variational step and then corrected during the perturbative step. For example, the α density matrix can be constructed via

$$D^\alpha = \langle \psi_0 | \hat{\rho}_\alpha | \psi_0 \rangle + 2 \langle \psi_0 | \hat{\rho}_\alpha | \psi_1 \rangle \quad (\text{S39})$$

with a similar equation for the β component. [S16] The variational density matrices are normalized such that the trace of each matrix will yield the number of electrons of a given spin.

$$\text{Tr}(D_{var}^\alpha) = N_\alpha \quad (\text{S40})$$

where N_α is the number of alpha electrons and D_{var}^α is the density matrix for the alpha electrons in the variational step. In the perturbative step, the trace of the perturbative density matrix tends to be on the order of 10^{-5} , as is the case for the oxygen atom at 3×10^{-5} , indicating a small but significant change in the density due to the perturbation. To preserve the total number of electrons, it is necessary to renormalize these matrices so that the total number of electrons is preserved.

$$\text{Tr}(D_{var}^\alpha + D_{EN}^\alpha) = N_\alpha \quad (\text{S41})$$

where D_{EN}^α represents the density matrix for the alpha electrons in the perturbation step. In order to get the calculation for CN to run with sufficiently tight epsilon values, it was necessary to parallelize it. The perturbative correction to the density matrix is not implemented in this highly parallel version of the code at this time. As a result, the density for CN comes from only the variational step. The perturbative energy correction for CN is still included in this manuscript to show that it is relatively small and therefore, the perturbative density correction would also be small.

TABLE XII. Total energy values with a breakdown into contributions from the variational and perturbative step and the values of ϵ_1 and ϵ_2 .

Compound	Variational Energy (Ha)	Perturbative Energy (Ha)	Total Energy (Ha)	ϵ_1 (μ Ha)	ϵ_2 (μ Ha)
Li	-7.4764	0.000	-7.4764	0	-
C	-37.8380	-0.0002	-37.8383	100	0.1
N	-54.5795	-0.0006	-54.5801	100	0.1
O	-75.0521	-0.0007	-75.0528	100	0.1
CH ₂	-39.1309	-0.0014	-39.1323	100	0.1
CN	-92.7006	-0.0052	-92.7058	50	0.05

-
- [S1] Wilhelm Magnus. On the exponential solution of differential equations for a linear operator. *Communications on pure and applied mathematics*, 7(4):649–673, 1954.
- [S2] Sandeep Sharma, Adam A. Holmes, Guillaume Jeanmairet, and C. J. Umrigar. Semistochastic heat-bath configuration interaction method: Selected configuration interaction with semistochastic perturbation theory. *J. Chem. Theory Comput.*, 13:1595–1604, 2017.
- [S3] Adam A. Holmes, C. J. Umrigar, and Sandeep Sharma. Excited states using semistochastic heat-bath configuration interaction. *J. Chem. Phys.*, 147:164111, 2017.
- [S4] Junhao Li, Matthew Otten, Adam A. Holmes, Sandeep Sharma, and C. J. Umrigar. Fast semistochastic heat-bath configuration interaction. *J. Chem. Phys.*, 149:214110, 2018.
- [S5] Kurt R. Brorsen. Quantifying multireference character in multicomponent systems with heat-bath configuration interaction. *J. Chem. Theory Comput.*, 16:2739,2388, 2020.
- [S6] Adam A. Holmes, Norm M. Tubman, and C. J. Umrigar. Heat-bath configuration interaction: An efficient selected configuration interaction algorithm inspired by heat-bath sampling. *J. Chem. Theory Comput.*, 12:3674–3680, 2016.
- [S7] Yuan Yao and C. J. Umrigar. Orbital optimization in selected configuration interaction methods. *J. Chem. Theory Comput.*, 17:4183–4194, 2021.
- [S8] Alan D. Chien, Adam A. Holmes, Matthew Otten, C. J. Umrigar, Sandeep Sharma, and Paul M. Zimmerman. Excited states of methylene, polyenes, and ozone from heat-bath configuration interaction. *J. Phys. Chem.*, 122:2714–2722, 2018.
- [S9] Duy-Khoi Dang, Leighton W. Wilson, and Paul M. Zimmerman. The numerical evaluation of Slater integrals on graphics processing units. *J. Comput. Chem.*, 43:1680–1689, 2022.
- [S10] Duy-Khoi Dang, Joshua A. Kammeraad, and Paul M. Zimmerman. Advances in parallel heat bath configuration interaction. *J. Phys. Chem.*, 127:400–411, 2023.
- [S11] Yohan Shao et al. Advances in molecular quantum chemistry contained in the Q-Chem 4 program package. *Mol. Phys.*, 113(2):184–215, 2015.
- [S12] Bjorn O. Roos and Peter R. Taylor. A complete active space scf method (casscf) using a density matrix formulated super-ci approach. *Chem. Phys.*, 48:157–173, 1980.
- [S13] Bjorn O. Roos. The complete active space scf method in a fock-matrix-based super-ci formulation. *Int. J. Quant. Chem.*, 18:175–189, 1980.
- [S14] David E. Woon and Thom H. Dunning Jr. Gaussian basis sets for use in correlated molecular calculations. v. core-valence basis sets for boron through neon. *J. Chem. Phys.*, 103:4572–4585, 1995.
- [S15] Kirk A. Peterson and Thom H. Dunning Jr. Accurate correlation consistent basis sets for molecular core-valence correlation effects: The second row atoms al-ar, and the first row atoms b-ne. *J. Chem. Phys.*, 117:10548–10560, 2002.
- [S16] Trygve Helkager, Poul Jorgensen, and Jeppe Olsen. *Molecular Electronic Structure Theory*. John Wiley & Sons, 2002.